Creep burst coincident with faulting in marble observed in 4D synchrotron X-ray imaging triaxial compression experiments

François Renard[1,2], Neelima Kandula[1], Jessica McBeck[1], Benoît Cordonnier[1]

[1] Physics of Geological Processes, The Njord Centre, Department of Geosciences, University of Oslo, Oslo, Norway

[2] University Grenoble Alpes, University Savoie Mont Blanc, CNRS, IRD, IFSTTAR, ISTerre, 38000 Grenoble, France

Corresponding author: François Renard (francois.renard@geo.uio.no)

Key Points:

- Transient creep bursts under constant stress conditions are detected in laboratory experiments
- The bursts correlate with an increase of dilatancy, including the opening and rotation of microfractures
- The macroscopically-detected bursts correlate with the microscopically-observed nucleation, growth, dilation and shearing of faults

Abstract

Faults in carbonate rocks show both seismic and aseismic deformation processes, leading to a wide range of slip velocities. We deformed two centimeter-scale cores of Carrara marble at 25°C, under in-situ conditions of stress of 2-3 km depth, and imaged the nucleation and growth of creeping faults using dynamic synchrotron X-ray microtomography with micrometer spatial resolution. The first sample was under a constant confinement of 30 MPa and no pore fluid. The second sample was under a confinement in the range 35-23 MPa, with 10 MPa pore fluid pressure. We increased the axial stress by steps until creep deformation occurred and imaged deformation in 4D during creep. The samples deformed with a steady-state strain rate when the differential stress was constant, a process called creep. However, for both samples, we also observed transient events that include the acceleration of creep, i.e., creep bursts, phenomena similar to slow slip events that occur in continental active faults. During these transient creep events, strain rates increase and correlate in time with strain localization and the development of system-spanning fault networks. In both samples, the acceleration of opening and shearing of microfractures accommodated creep bursts. Using high-resolution time-lapse X-ray micro-tomography imaging, and digital image correlation, during triaxial deformation allowed quantifying creep in laboratory faults at sub-grain spatial resolution, and demonstrates that transient creep events (creep bursts) correlate with the nucleation and growth of faults.

Plain Language Summary

Active faults may slip at velocities close to one meter per second during earthquakes, but may also slip at much slower rates, in creep. Sometimes such creep is continuous in time, sometimes it is transient and occurs as creep bursts, also called slow slip events. Using state of the art synchrotron X-ray imaging of core samples of Carrara marble, we identified such creep bursts under conditions of pressure and temperature similar to that in the Earth's upper crust. Our 4D imaging technique allows seeing through the sample and characterizing the microphysical processes that produce creep bursts. Results show that acceleration of microfractures nucleation, growth and coalescence in the sample may lead to the formation of system-spanning faults that coincide in time with the macroscopically-observed creep burst. These results demonstrate that creep bursts do not only correspond to slow slip events on active preexisting faults, but may also indicate the development of new active faults.

1 Introduction

Fault slip can reach velocities on the order of a meter per second during earthquakes, or much slower velocities when displacements occur over hours to weeks. Events of such slower velocities, known as creep transients, or slow slip events when applied to active faults, indicate a permanent deformation whose rate ranges between the tectonic loading rate and earthquake rates (e.g., Bürgmann, 2018). At least two physical mechanisms have been linked to creep in the Earth's upper crust. Brittle creep can occur by the chemically-activated slow growth and coalescence of microfractures (Scholz, 1968; Brantut et al., 2013). Alternatively, pressure solution creep arises from the coupling between mechanical and chemical forces at the grain scale such that mass transfer through dissolution and precipitation processes controls volumetric deformation (e.g., Rutter, 1976; Gratier et al., 2013). The rheological laws of these two

mechanisms describe strain rate as a function of a series of mechanical, chemical and petrophysical parameters, such as stress, temperature, rock composition, grain size and fluid composition.

When the system is subjected to less than 90% of failure stress, the creep rate is usually constant through time (e.g Lockner 1993). When approaching failure, the coalescence of microfractures may lead to an exponential or power law increase of creep rate, until catastrophic failure (Reches and Lockner, 1994; Main, 2000; Amitrano and Helmstetter, 2006). In creeping faults, the creep rate may be constant through time, corresponding to steady-state slip. However, transient stages of the acceleration of slow displacements in continental faults have been observed in borehole strain meters (Linde et al., 1996) and in geodetic data (Crescentini et al., 1999; Jolivet et al., 2013). Such creep bursts, or slow slip events, are observed as periods of the increase of slip rate before the fault either becomes locked again or continues to creep at a lower rate. Creep rates measured in major continental faults using time-lapse satellite interferometry indicate that slow slip events can have a wide range of slip surface areas and durations (Jolivet et al., 2015). Some slow slip events can occur on a fault tens of years after a major earthquake (Aslan et al., 2019). Slow slip events can also trigger seismicity (Lohmann and McGuire, 2007) and may control the nucleation process before some major earthquakes (Bouchon et al., 2011). Creep transients induced by anthropogenic fluid injections can also trigger seismicity at the meter to kilometer scales (Guglielmi et al., 2015; Wei et al., 2015).

Because creep deformation can precede seismic failure in rocks, an acceleration of creep may indicate an approaching catastrophic event (e.g., Kranz, 1980). This recognition led to the concept of predicting the time to failure of major earthquakes, landslides, and volcanic eruptions (Voigt, 1989; Main, 1999). The creep evolution of some landslides before failure follows this concept (Carlà et al., 2019). However, transient slip acceleration does not always indicate the onset of a catastrophic failure, as for the Mud Creek landslide in California, for example (Handwerger et al., 2019).

Observations of rock creep in the crust have motivated the development of laboratory experiments to measure the process and propose rheological laws. Since early creep experiments on sedimentary rocks (Griggs, 1939) and granodiorite and gabbro rocks (Lomnitz, 1953), series of laboratory experiment studies have characterized brittle creep in various rocks, such as granite (Kranz and Scholz, 1977; Lockner and Byerlee, 1977; Ross et al., 1983; Kie et al., 1989; Lockner, 1993; Lei et al., 2000), basalts (Heap et al., 2011), amphibolite (Satoh et al., 1996), marble (Yang et al., 2015; Quintanilla-Terminel and Evans, 2016; Tal et al., 2016; Liu and Shao, 2017) and sandstone (Ngwenya et al., 2000; Baud and Meredith, 1997; Tsai et al., 2008; Shengqi and Jiang, 2010). In all of the experiments that reached failure, an acceleration of creep and an increase of acoustic emissions occurred before failure, suggesting the predictability of the time to failure. However, experimental techniques that use acoustic emission recording are blind to aseismic deformation mechanisms at the grain scale because they can only detect the seismic component of deformation. This limitation challenges attempts to estimate the time to failure from microstructural parameters, such as the evolving fracture network geometry, and the validation of theoretical studies on creep in rocks.

In creep experiments under constant stress conditions, the macroscopic axial strain rate may increase or decrease, often with three main stages until macroscopic failure (e.g., Lockner, 1993). First, primary creep occurs with an initial non-linear increase in strain with time (Figure 1). Next, the onset of secondary creep occurs as a decrease in strain rate, producing a quasi-linear

relationship between strain and time. Finally, tertiary creep occurs as an acceleration of strain with an exponential or power law dependence that ends with catastrophic failure (Figure 1). In the present study, we show in laboratory experiments that the stage of tertiary creep may contain transient accelerations of strain, i.e., creep bursts, superimposed on the exponential or power law trend of strain and time.

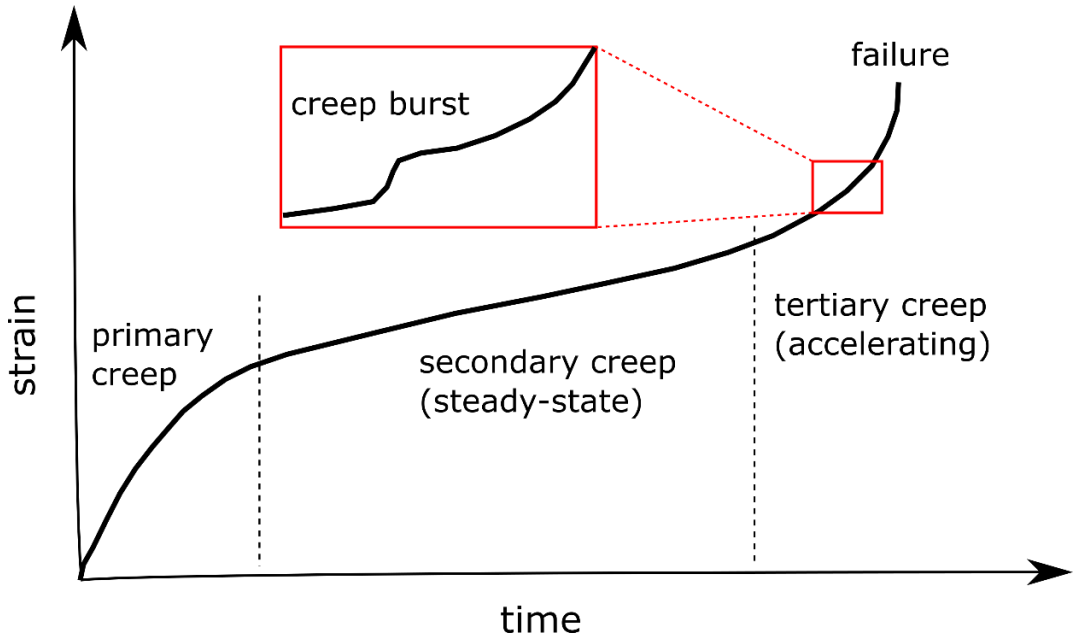

Figure 1: Sketch of the evolution of strain until sample failure during a laboratory creep test, with three stages: primary, secondary and tertiary creep. The inset shows a transient acceleration of strain, also called creep burst.

A key question in studying creep processes is how mechanisms at the grain scale, such as microfracturing, interact at mesoscopic and then macroscopic scales to produce the observed permanent creep or transient creep bursts observed in the upper crust (e.g. Brantut et al., 2013). The rock deformation experiments in the creep regime with dynamic X-ray microtomography imaging (4D μCT), decribed in the present study, enable linking the macroscale behavior and the microscale processes under in-situ conditions of the upper crust. This technique allows seeing within a rock sample while it deforms, with spatial resolution below the grain scale. Here, we show that the nucleation and growth of microfractures accommodate steady-state creep under constant stress conditions. A creep burst detected during each experiment coincides in time with the nucleation and propagation of system-spanning fault networks. We track the microstructural geometric properties of the microfractures and the local incremental strain deformation with digital volume correlation. Results allow characterizing the evolution of porosity, dilation, compaction and shear strain before, during, and after the creep burst event.

2 Materials and Methods

2.1 Dynamic synchrotron in-situ experiments

The rock samples used here are cylindrical cores, 5 mm in diameter and 10 mm in height, drilled from a block of Carrara marble. They come from the same block used in the eperiments of rock failure performed in Kandula et al. (2019). Carrara marble is a coarse-grained, nearly pure calcite rock with grain size in the range of 100-200 micrometers and initial (undeformed) porosity less than 1%. Each core sample was inserted into a Vitton jacket and between two stainless steel pistons. The interfaces between the samples and the piston were not lubricated. This sample assembly was mounted into the Hades triaxial rock deformation apparatus. The details of the apparatus, including sketch and operating conditions are described in Renard et al. (2016). This apparatus is installed on the beamline ID19 at the European Synchrotron Radiation Facility (ESRF) and is used to perform 4D μCT imaging during rock physics experiments at in-situ conditions of the upper crust. Table 1 describes the experimental conditions for the two samples. Figure 2 shows the axial stress, confining pressure, differential stress and axial strain as a function of time. Experiments were performed at the room temperature of the hutch of beamline ID19 at ESRF, in the range 23-25 °C.

The μCT data were acquired by rotating the Hades rig, with the sample inside, over 180° and taking either 1800 (sample M83) or 1600 (sample M84) radiographs using the full white beam of the synchrotron. In these experiments, the Hades rig acts as a filter for X-rays so that an equivalent energy of 85 keV crosses the sample. Each scan duration was two minutes with another two minutes between scans. As a result, we acquired μCT scans every four minutes. Tomographic reconstruction is performed using the program PyHST2 (Mirone et al., 2014). The voxel size is 6.5 μm^3 and the spatial resolution is 6.5 μm. The tomograms map the three-dimensional X-ray attenuation in the samples, with the calcite grains having a stronger attenuation (light gray values) than air-filled voids (dark gray values). Each tomogram of the rock sample contained around $7.1 \cdot 10^8$ voxels.

Table 1: Experimental conditions for samples M83 and M84. P_c: confining pressure; P_p: pore fluid pressure; P_{oring}: differential pressure due to friction in the O-rings of the rig; T: temperature; σ_f: differential stress at macroscopic failure; ε_y: macroscopic axial strain at yield; nb. XCT: number of 3D microtomography tomograms acquired during the experiment; duration: total duration of the experiment from the onset of loading to unloading.

sample	**P_c (MPa)**	**P_p (MPa)**	**P_{oring} (MPa)**	**T (°C)**	**σ_f (MPa)**	**ε_y**	**nb. XCT scans**	**duration (hours)**
M83	30	0	10	23	154	0.036	162	6.7
M84	35 → 23	10	2	25	180	0.025	100	9.7

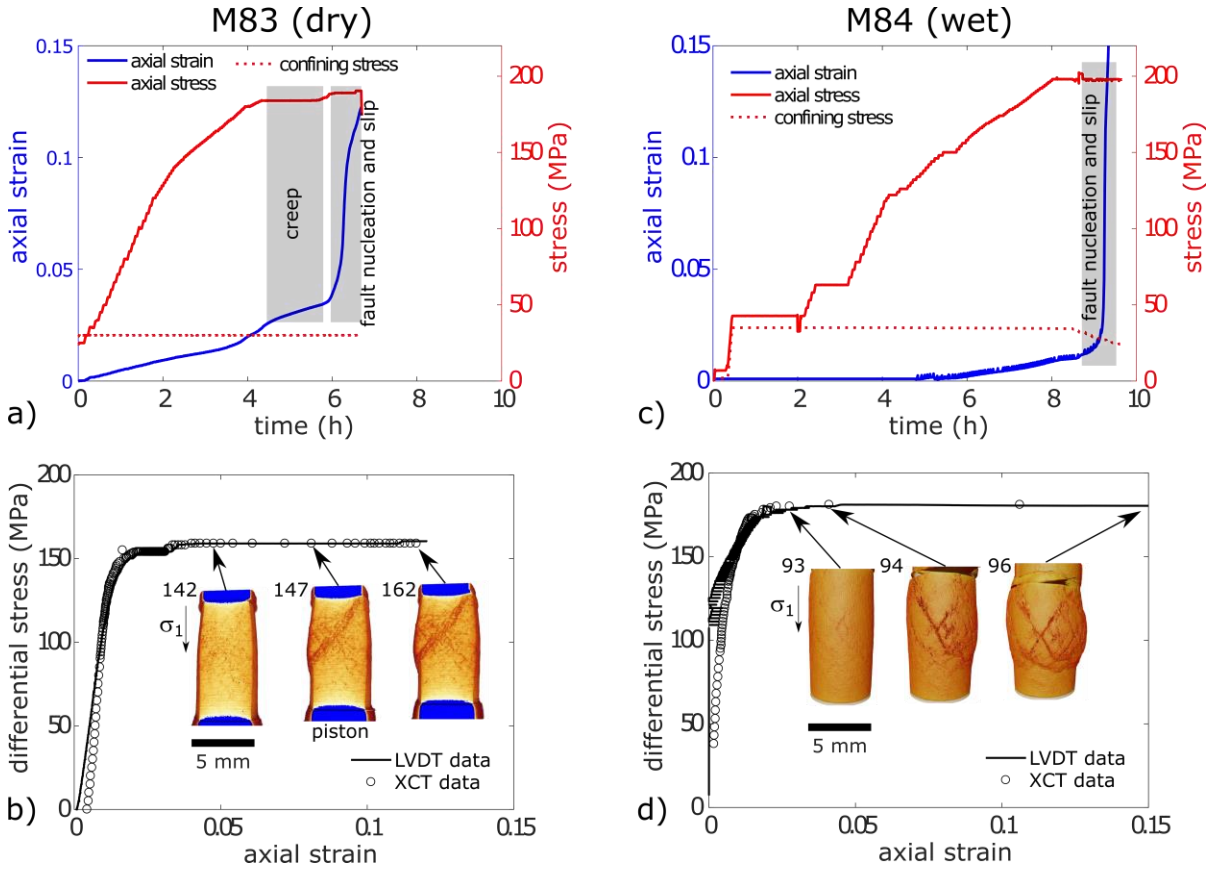

Figure 2: Stress, strain, and X-ray tomography acquisitions for the two samples of Carrara marble M83 (no pore fluid, left) and M84 (with pore fluid, right). Axial strain, axial stress and confining stress as a function of time for experiment M83 (a) and M84 (c). The shaded rectangular areas correspond to periods where the stresses are constant and the sample deforms either by volumetric creep (i.e. without localization at the sample scale) or through the slow nucleation and growth of a fault network during a creep burst. b, d) The axial strain is measured with two independent techniques, with the displacement transducer (LVDT), and from the 3D tomograms (XCT). Each circle indicates the acquisition of a 3D tomogram. Insets show views of the sample and fault formation. Numbers indicate the number of the 3D tomogram. For experiment M83, around twenty tomograms were acquired during fault network nucleation and formation (i.e. creep burst). For experiment M84, only three tomograms were acquired during macroscopic fault formation (i.e. creep burst). The largest principle stress, σ_1, is parallel to the axis of the cylindrical sample.

2.2 Stress control and axial strain measurement

For both samples, the axial stress, σ_1, confining pressure, P_c, and pore pressure, P_p, are controlled by independent pumps connected to the Hades rig. The differential stress in the sample is $\sigma_{diff} = \sigma_1 - (P_c - P_p) - P_{oring}$, where P_{oring} is pressure caused by the friction of the O-rings of the rig (Table 1). For the first sample, M83 (dry), the confining pressure was constant and equal to 30 MPa, with no fluid pressure. The axial stress was increased by steps of 5

MPa below a differential stress of 100 MPa, then by steps of 2 MPa between differential stresses of 100 MPa and 120 MPa, then steps of 1 MPa until a differential stress of 154 MPa was reached. The sample was left under a constant differential stress of 154 MPa and then started to creep (left gray rectangle in Figure 2a). A first series of 3D radiographs was then acquired (Figure 3a). Then, the differential stress was increased to 159 MPa, cycled four times between 158 and 159 MPa to enhance creep, and left constant at 159 MPa for 100 minutes (right gray rectangle in Figure 2a), during which a fault network propagated across the sample (Figure 3b). This fault propagation corresponds to the creep burst observed macroscopically (Figure 3b). Around twenty tomograms were acquired during this event, between scan numbers 139 and 162 (e.g., Figures 2b, 3b).

For the second sample, M84 (wet), the initial confining pressure was set to 35 MPa during most of the experiment and then reduced to 23 MPa at the end of the experiment. The fluid pressure was constant and equal to 10 MPa. The axial stress was increased by steps of 5 MPa below a differential stress of 93 MPa, then by steps of 2 MPa between differential stresses of 93 MPa and 133 MPa, then steps of 1 MPa until a differential stress of 165 MPa was reached. At this stress level, the axial stress was 200 MPa, the maximum available on the Hades rig. We acquired a series of tomograms, and measured negligible creep of the sample. Because of the limited time available at the ESRF for this experiment, the confining pressure was reduced by steps of 1 MPa to 23 MPa to increase creep rate. At 23 MPa confining stress, corresponding to 172 MPa differential stress, several faults nucleated in the sample and propagated within four minutes, resulting in macroscopic failure (gray rectangle in Figure 2c, Figure 4). Only three tomograms were acquired during this faulting episode, from scan numbers 94 to 96 (Figure 2d). Because of sample deformation during these scans, the 3D volumes are blurred and so we could not robustly quantify the porosity. The movies S1 and S2, provided as supplementary material, display time-lapse 3D rendering of the samples during the experiments.

For both samples, we measured the macroscopic axial strain by two independent techniques. First, a linear variable differential transformer (LVDT) displacement sensor installed on the Hades rig measures the axial displacement of the upper piston, which records the shortening of the sample (LVDT data in Figures 2b, 2d). This data is corrected from the elastic deformation of the rig. Second, from the 3D tomograms we measured the height of the sample as a function of time (XCT data in Figures 2b, 2d). Both measurements techniques show similar results. The experiments were stopped after an axial strain of 12% (sample M83) or 60% (sample M84, after failure) were reached.

2.3 Porosity imaging and quantification

Because of the contrast in X-ray attenuation between the calcite grains of the Carrara marble and the air-filled voids, we can separate the microfractures and pores from the solid grains (Figures 5, 6). This procedure (i.e., segmentation) allows extracting the porosity of each scan. In our samples, the initial porosity detected by the segmentation procedure is less than 0.05%. Thus, most of the porosity that subsequently develops arises from microfracture propagation. We used a simple workflow to extract the microfracture by segmenting the data of sample M83. First, each tomogram was filtered using a non-local mean filter (Buades et al., 2005) to reduce noise in the data and thus enhance boundaries between grains and voids. Then a cylindrical mask was used to select a subvolume centered in the rock sample and comprising 63% of its volume, thereby reducing boundary effects by removing data near the jacket and the

pistons. Then, a threshold in gray level of 13800 was applied. All voxels below this value are considered voids and all voxels above it are considered grains.

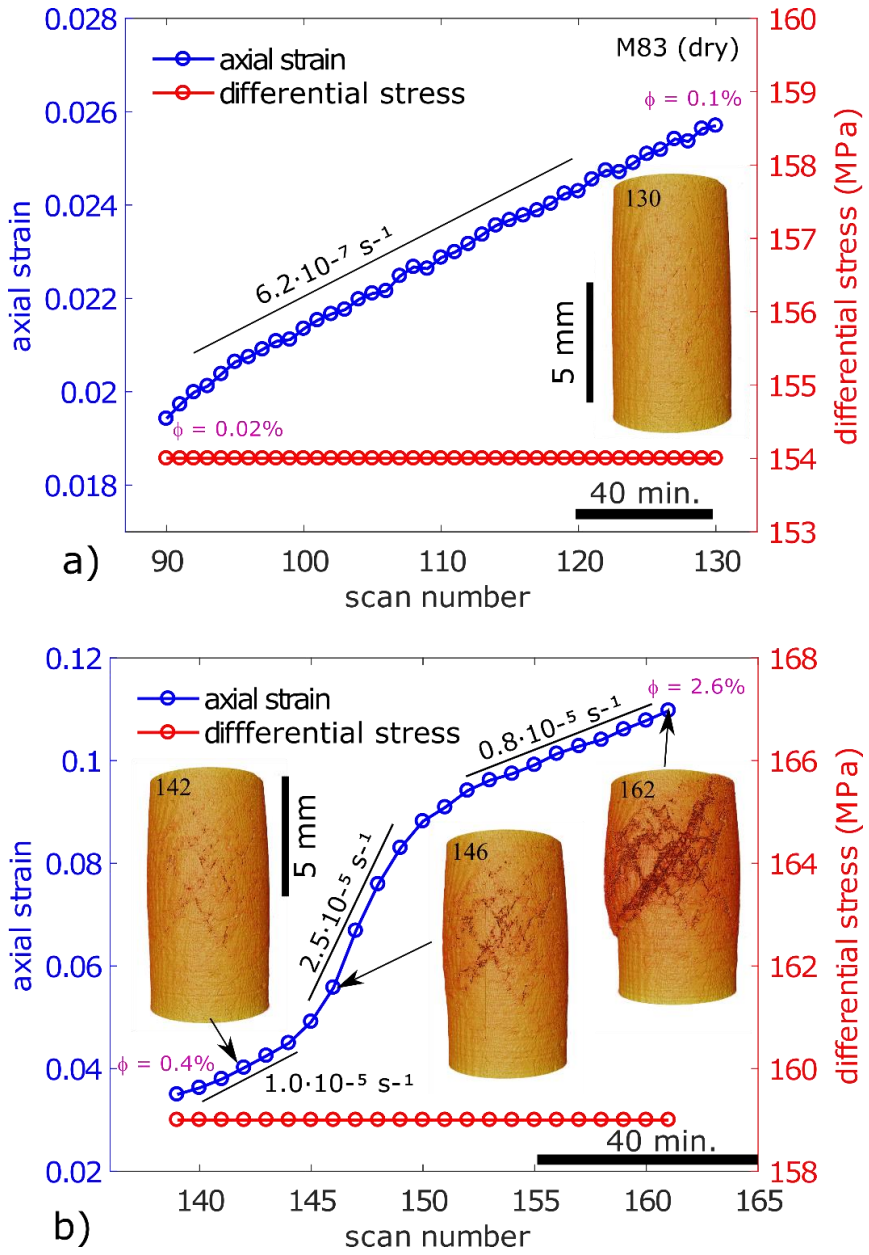

Figure 3: Macroscopic axial strain and differential stress for each scan acquired of sample M83 (no pore fluid) in the periods indicated by gray rectangles in Figure 2a: a) The period with a linear increase of strain with time corresponds to sample deformation by secondary creep. b) The period with a transient acceleration of creep (i.e., creep burst between scans 140 and 150) corresponds to the nucleation and growth of a system-spanning fault network. Each circle indicates the acquisition of a 3D tomogram. Insets show 3D views of the sample. Horizontal black bars show a duration of 40 minutes. The porosity of the sample, ϕ, is indicated at the beginning and end of each curves.

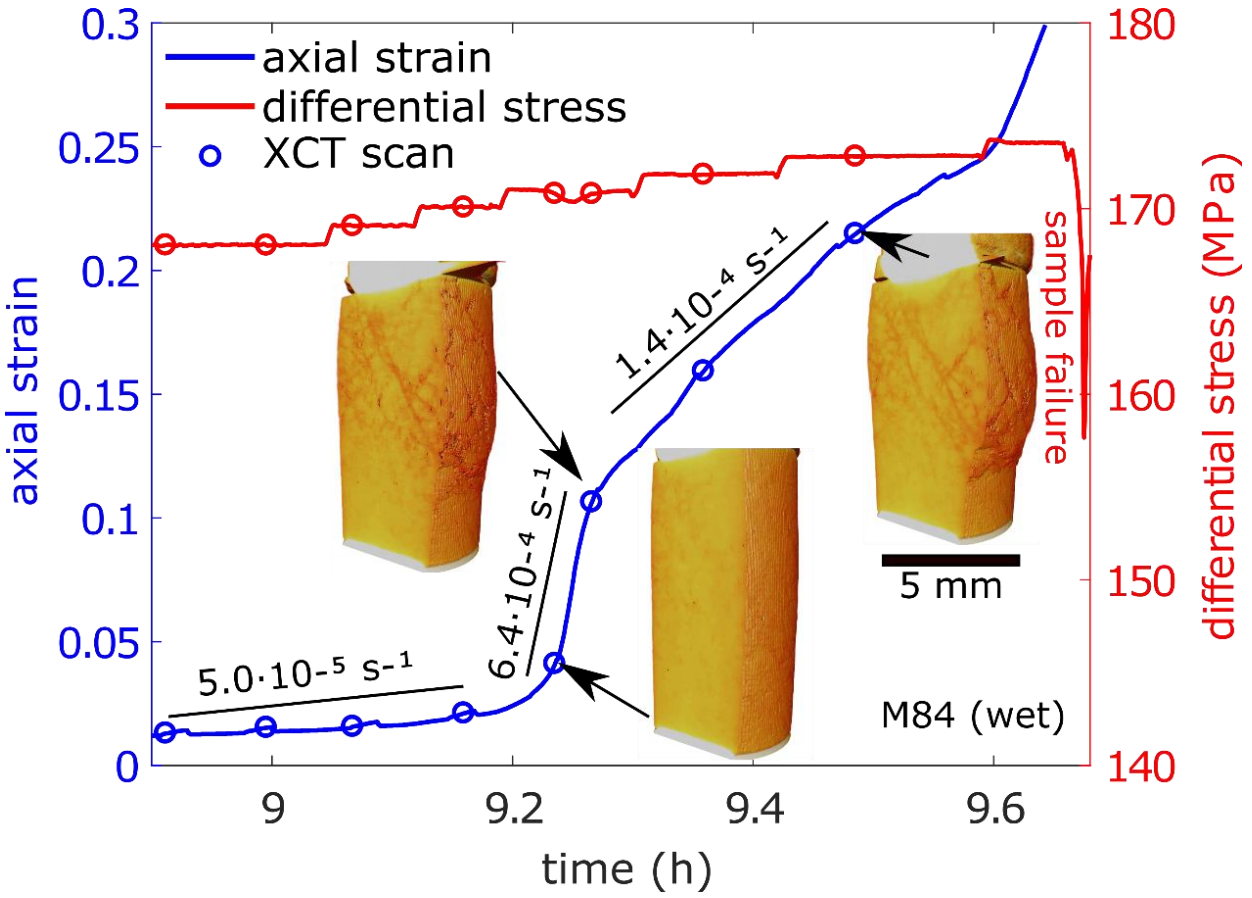

Figure 4: Axial strain and differential stress as a function of time for sample M84 (with pore fluid) in the period indicated by gray rectangles in Figure 2b. The transient acceleration of creep (i.e., creep burst between 9.2 and 9.4 h), observed macroscopically, corresponds to the nucleation and growth of a fault network that hosts system-spanning conjugate faults, observed with X-ray tomography. Each circle indicates the acquisition of a 3D tomogram. Insets show 3D views of the sample. Local macroscopic axial strain rates are indicated above the axial strain curve.

We then calculated the evolution of porosity (Figure 7a) and the evolutions of the number of microfractures, mean volume of microfractures, and mean distance between microfractures during the creep burst (Figure 8). To characterize the spatial variability of the porosity along the axis of the core sample, we divided the tomograms into a series of vertical layers, each 130 micrometers thick (20 voxels), calculated the porosity in each layer, and plotted the evolution with time (Figure 7b).

To characterize the shape of the microfractures (Figure 9), we calculated the covariance matrix of each microfracture, from which the three eigenvalues λ_1, λ_2, and λ_3, represent the three principle axes of the microfracture (inset in Figure 9c). The mean values of these eigenvalues, the evolutions of the angle ϕ, between λ_1 and the vertical direction, and the angle ϕ_2, between λ_3 and the vertical direction are displayed in Figures 9a and 9b. We also calculated the distribution and the average of the microfracture flatness, defined by the ratio λ_3/λ_2, with flat objects having a flatness close to zero (Figures 9c, 9d).

2.4 Digital volume correlation

To characterize the volumetric and shear strain evolution in sample M83, we calculated the incremental 3D internal displacement vectors between successive scans using digital volume correlation analysis, implemented in the software TomoWarp2 (Tudisco et al., 2017) and following the same procedure as previous analyses (McBeck et al., 2018; Renard et al., 2019). Digital volume correlation calculates the displacement vectors inside the sample at the locations of points called nodes, and uses a cubic correlation window around each node to calculate the incremental displacement done between two successive 3D scans. The node spacing was 20 voxels (130 μm) and the correlation windows size was 10 voxels (130 μm).

Using the incremental displacement fields calculated between two tomograms, we examine both the volumetric and shear components of the strain by calculating the divergence and curl of the displacement fields, respectively. The divergence is proportional to the first invariant of the incremental strain tensor and thus represents a measurement of local volume changes. Positive divergence indicates local dilation and negative divergence indicates local contraction. The curl is a vector that characterizes the rotational component of the displacement field. The norm of this vector is used here as a proxy for incremental shear strain. In a Cartesian coordinate system where the z-axis is vertical and parallel to the core sample axis, and the x- and y-axis are perpendicular, horizontal and arbitrarily selected, a positive curl indicates right-lateral shear strain, and a negative curl indicates left-lateral shear strain with respect to the coordinate system.

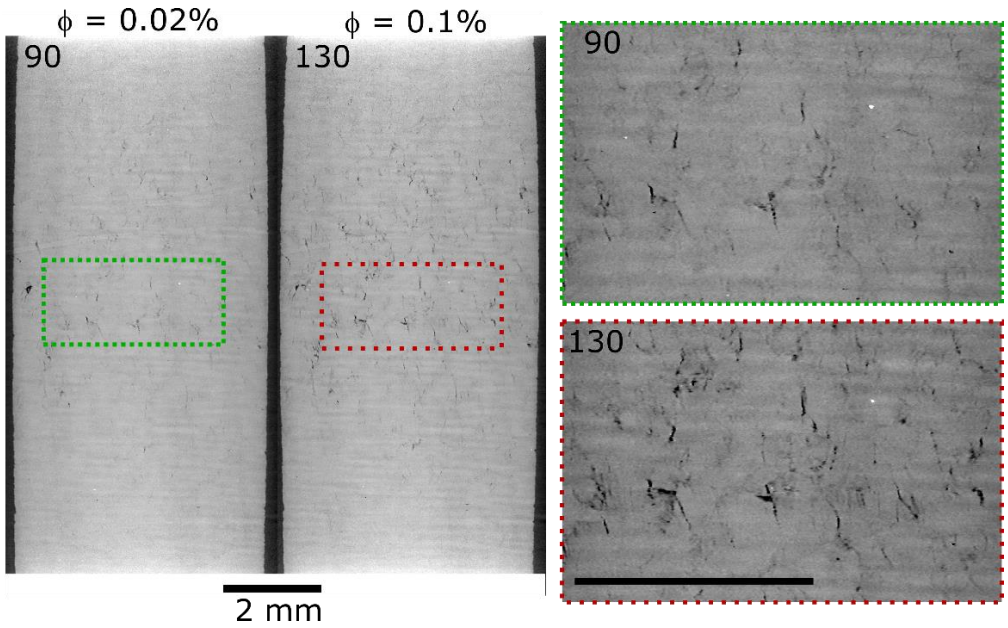

Figure 5: Two-dimensional slices aligned parallel to the maximum compressive stress in sample M83 (dry) when the differential stress was constant and equal to 154 MPa (scan numbers 90 and 130). Figure 3a shows the loading conditions of each scan. The gray scale of scans indicates X-ray attenuation, with darker shades corresponding to air-filled voids. Between these two scans, the porosity increased from 0.02% to 0.1% (Figure 3a) and the sample dilated via the nucleation and growth of microfractures. Scale bars are both 2 mm.

To visualize and quantify the strain increments we proceed in two steps. First, we show the localization patterns of the high (>95th percentile) incremental strain values (Figure 10, Movie S3). Second, we show the evolution of the cumulative values of these values with time, as deformation progresses (Figure 11). We show the cumulative values, rather than the incremental strain values, in order to compare this evolution to the trends in porosity, which is a cumulative property.

3 Results

3.1 Macroscopic strain and deformation pattern

The macroscopic differential stress and axial strain relationships show mechanical behavior typical of a triaxial deformation test during the initial stages when axial stress was increased (Figure 2). In the first step, the differential stress versus axial strain is nonlinear, concave upward, due to the closure of voids and the settling of the sample between the two pistons. The second step includes a linear increase of axial strain with differential stress. The third stage begins when a yield point is reached after around 2-3% axial strain (Table 1), followed by a fourth stage with strain hardening during which microfractures grow under constant differential stress (Figures 2b, 2d). We defined the yield point when a deviation of 3% from linearity occurs in the stress-strain curve. The fourth and final stage includes an acceleration of macroscopic creep driven by microfracture propagation and coalescence under either constant differential stress (sample M83) or slightly increasing differential stress (M84). For both samples, conjugate sets of faults developed in the sample (insets in Figure 2, Movies S1, S2). The main difference between the two samples is that for sample M83, deformed without pore fluid, the conjugate faults developed in about forty minutes. In contrast, in sample M84, including water, the faults became system-spanning in four minutes. Because we could acquire only three scans of sample M84 (wet) during fault initiation and propagation (Movie S2), and the propagation of microfractures blurred the scans, we do not characterize the porosity and incremental strain evolution of this sample in the following analysis. We focus this analysis on sample M83 for which we acquired several tens of tomograms during creep deformation at constant differential stress (Movie S1), which did not include significant fracture propagation or deformation during scan acquisition.

Figure 3 shows two periods of deformation of sample M83 (dry), corresponding to the gray rectangles indicated in Figure 2a. Under a constant differential stress of 154 MPa (scans 90 to 130), the sample creeps at a constant strain rate close to $6.2 \cdot 10^{-7}$ s^{-1} (Figure 3a), between scans 90 and 130. The nucleation and growth of microfractures produces the macroscopic creep (Figure 4). Twinning at the grain scale could accommodate part of the deformation. However, we could not identify this mechanism with the X-ray microtomography data. The quasi-linear trend in the increase of strain with time suggests that this stage can be defined as secondary creep (Figure 1).

Under a differential stress of 159 MPa (scans 139-162), an increase of axial creep rate from 10^{-5} to $2.5 \cdot 10^{-5}$ s^{-1}, defined as a creep burst, is observed from scans 140-150 (Figure 3b). The creep acceleration correlates in time with the nucleation and growth of a fault network that spans the rock core, including smaller conjugate faults (Figure 6, Movie S1). The sample-spanning fault network slips at a velocity in the range 0.4-1.8 micrometers per second, measured by the displacement along the main fault between scans 140-150. From scans 139-142, the

porosity increases, signaling an acceleration of fracture dilation (Figure 7a). Then the fractures that later comprise the system-spanning network begin to develop at scan 144, and continue to propagate until scan 150 (Figure 6). Between scans 150-162, the main fault network spans the system and the macroscopic strain rate decreases from $2.5 \cdot 10^{-5}$ s^{-1} to $0.8 \cdot 10^{-5}$ s^{-1}.

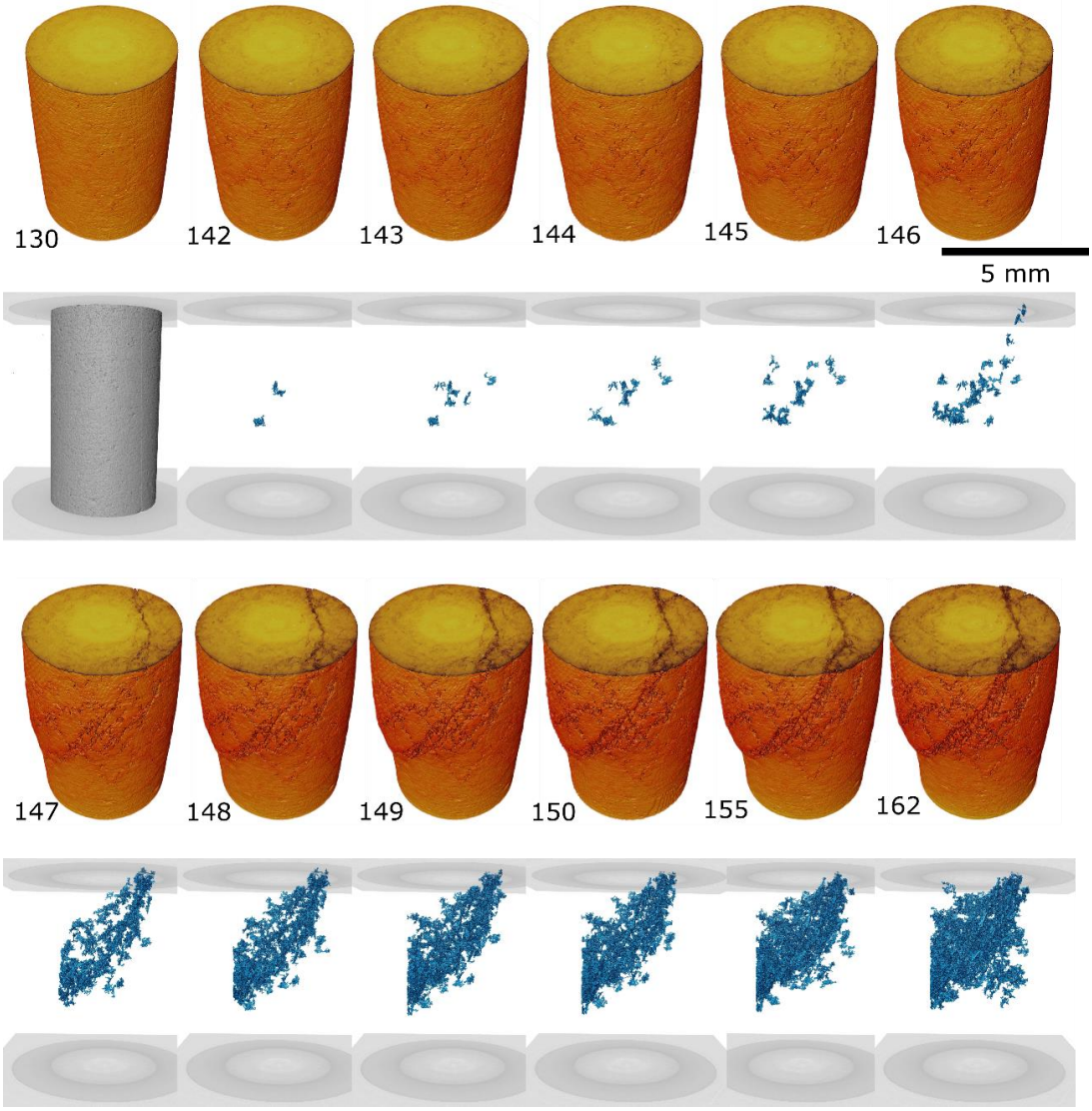

Figure 6: Series of three-dimensional views of sample M83 during the creep burst that led to the formation of a fault network under a constant differential stress of 159 MPa. Figure 3b shows the loading conditions of each scan number. Yellow-orange cylinders show 3D views of the sample, with fractures in darker colors. Blue figures show all the microfractures with volumes greater than 10^4 voxels. Around scan 142, the number of microfractures with volume above 10^4 voxels increase. The system-spanning fault network begins to develop between scans 140 to 150, leading to the formation of an offset along the sample boundary. For scans 150-162, this offset does not increase whereas the macroscopic axial strain increases, indicating mainly volumetric deformation in the core. The time between each scan is 4 minutes.

In sample M84 (wet), the strain rate at 170 MPa differential stress is equal to $5.0 \cdot 10^{-5}$ s^{-1} and deformation occurs by the nucleation of microfractures in the volume (Figure 4). After 9.2 hours, a creep burst starts with a strain rate of $6.4 \cdot 10^{-4}$ s^{-1} and lasts for four minutes. During this period, several conjugate faults develop and accommodate most of the deformation. The slip rate measured on the main faults, using the tomography data, between 9.24 and 9.28 hours is in the range 1.5-2.5 micrometers per second. After this creep burst, the strain rate decreases to $1.4 \cdot 10^{-4}$ s^{-1} until the sample failed at 9.7 hours (Figure 4).

3.2 Evolution of porosity

The porosity in sample M83 (dry) evolves during deformation (Figure 7). Microtomography reveals that fault growth occurs as the formation of a zone of increased porosity in the top half of the sample (Figures 6, 7a). This dilating volume propagates across the sample until it reaches the boundary of the rock core. The porosity of the entire sample increases from less than 0.5% before deformation to 2.5% after the fault network spans the core (Figure 7a). After the fault network has crossed the sample, the strain rate decreases. The time evolution of the porosity along a vertical profile in the sample shows that porosity increases mainly in the middle of the sample, far from the two pistons (Figure 7b). Above the fault network, the porosity increases with time during fault propagation (scans 139-150) and then stops increasing. Porosity continues to increase in the lower part of the sample (scans 150-162), below the fault network, after it has stopped propagating.

Segmenting the voids (fracture and pores) from the solid rock produce evolving statistics of microfracture geometry (Figures 8, 9). During the steady-state creep stage (scans 90-130 in Figure 3a), the mean values of the three eigenvalues of the covariance matrix, λ_1, λ_2, and λ_3, increase slowly (Figure 9a). Idealizing a microfracture as a perfect ellipsoid, the three eigenvalues correspond to the three main axes of the ellipsoid, with the smallest eigenvalue, λ_3, corresponding to the fracture aperture. During scans 90-130, a phase a secondary creep before the creep burst, the average angle between the largest principle axis of the microfractures, λ_1, and the horizontal plane, ϕ, remains constant, around 64° (Figure 9b). The angle between the smallest principle axis of the microfractures (λ_3) and a horizontal plane, ϕ_2, also remains constant, above 70°. This high value of the angle ϕ_2 indicates that the smallest dimensions of the microfractures is almost perpendicular to the vertical direction, and thus that the long axes of the microfractures are oriented almost parallel to σ_1. The flatness, corresponding to the ratio between the smallest and the intermediate eigenvalues of the microfractures is constant and equal to 0.2 (Figure 9c), indicating that the microfractures are generally flat objects, with a geometry similar to that of a penny shape.

During the stage of the experiment with the fastest rate of macroscopic creep (scans 139-150 in Figure 3b), i.e., the creep burst, the number and mean volume of microfractures increase (Figure 8). As a consequence, the mean distance between microfractures decreases (Figure 8b). The three eigenvalues of the microfractures and their flatness increase (Figures 9a, 9c, 9d). This observation indicates that the microfractures grow in length and width, explaining the increase of porosity and thus dilatancy. Concurrently, the mean orientation of the microfractures evolves: the angle ϕ increases to 68°, while the angle ϕ_2 decreases to 60° (Figure 9b). Because the flatness of the voids is small, less than 0.3, these voids have a flat shape with λ_1, $\lambda_2 >> \lambda_3$. With such geometry, the longest axis of the voids could be either vertical or horizontal, with an angle ϕ than

can therefore be either close to 90° or close to 0° for a vertical microfracture. Therefore, the angle ϕ_2 of the smallest axis, λ_3, is the most relevant geometrical parameter to estimate the orientation of penny-shaped microfractures. High angles of ϕ_2 indicates that the aperture of the fracture is perpendicular to σ_1, or that the penny-shaped fracture is close to being vertical (inset in Figure 9b). The evolution of ϕ_2 observed on Figure 9b shows a rotation of the microfracture orientation, with the smallest dimension oriented at 60° to σ_1. This orientation corresponds to one of the other two axes of the microfractures oriented at 30° to σ_1, the optimal orientation for shear faulting when considering an internal friction coefficient equal to 0.6 (Anderson, 1905).

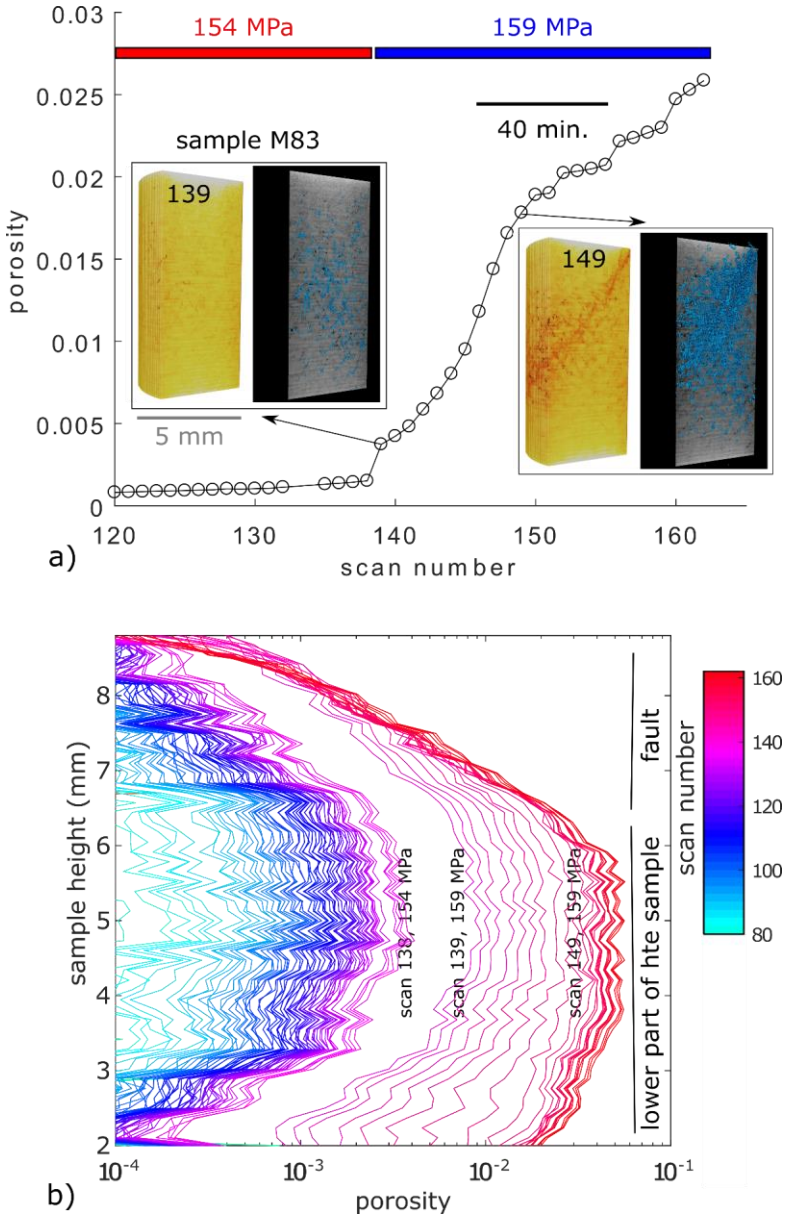

Figure 7: a) Evolution of porosity in sample M83 as a function of scan number during fault network development. Insets show a three-dimensional rendering (left) where color intensity represents X-ray attenuation (darker shades correspond to pores, with less attenuation) and

segmentation of the pores (right, porosity in blue) at two time steps. Before fault network growth (scan 139), porosity is mainly concentrated in the central part of the sample. After the network reaches the sample boundaries (scan 149), porosity becomes concentrated around the fault plane. The jump in porosity between scans 138 and 139 is due to an increase of imposed differential stress from 154 to 159 MPa. b) Evolution of porosity with time (scan number) along the vertical axis of the sample. The porosity increases mostly in the middle of the sample and less near the pistons at the top and bottom boundaries. After scan 139, the differential stress remained constant until the end of experiment (scan 162). The fault network developed in the upper part of the sample (scans 139-149), while porosity continued to increase in the lower part of the sample and we interpret that shearing prevented porosity increase in the fault.

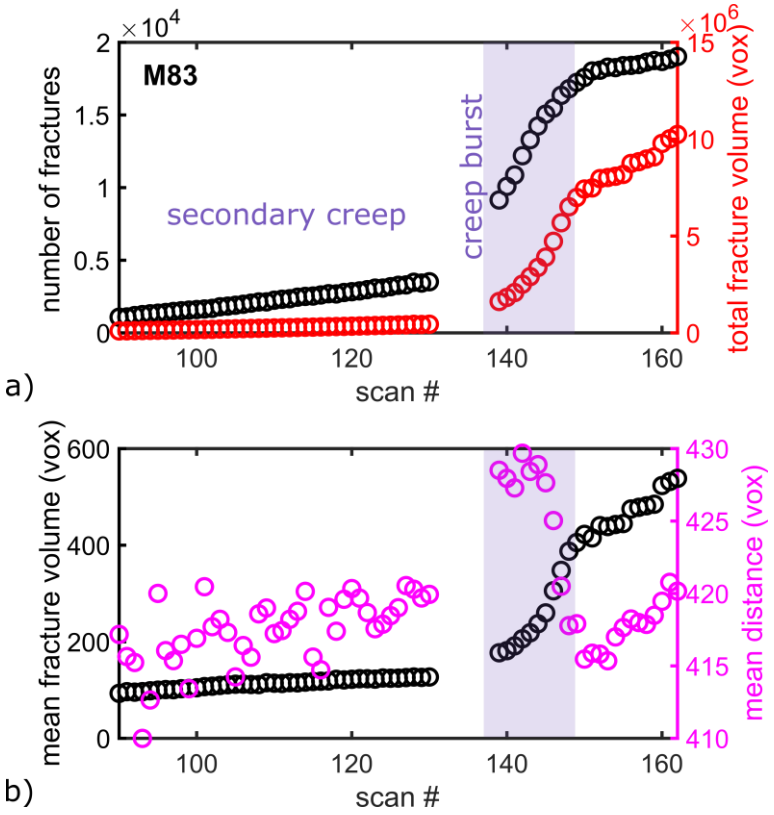

Figure 8: Evolution of the number of microfractures and total microfracture volume (a), and the mean microfracture volume and mean distance between microfractures (b) as a function of scan number. During the secondary creep phase, the total number of fracture increases, whereas the total fracture volume remains constant. During the creep burst (scans 139-150, shaded rectangle), the number and the mean volume of microfractures increase whereas the mean distance between microfractures decreases. Following the creep burst, the number of fractures, mean fracture volume, and mean distance between fractures all tend to plateau, indicating the slowing or stalling of fracture network development (i.e., fault locking).

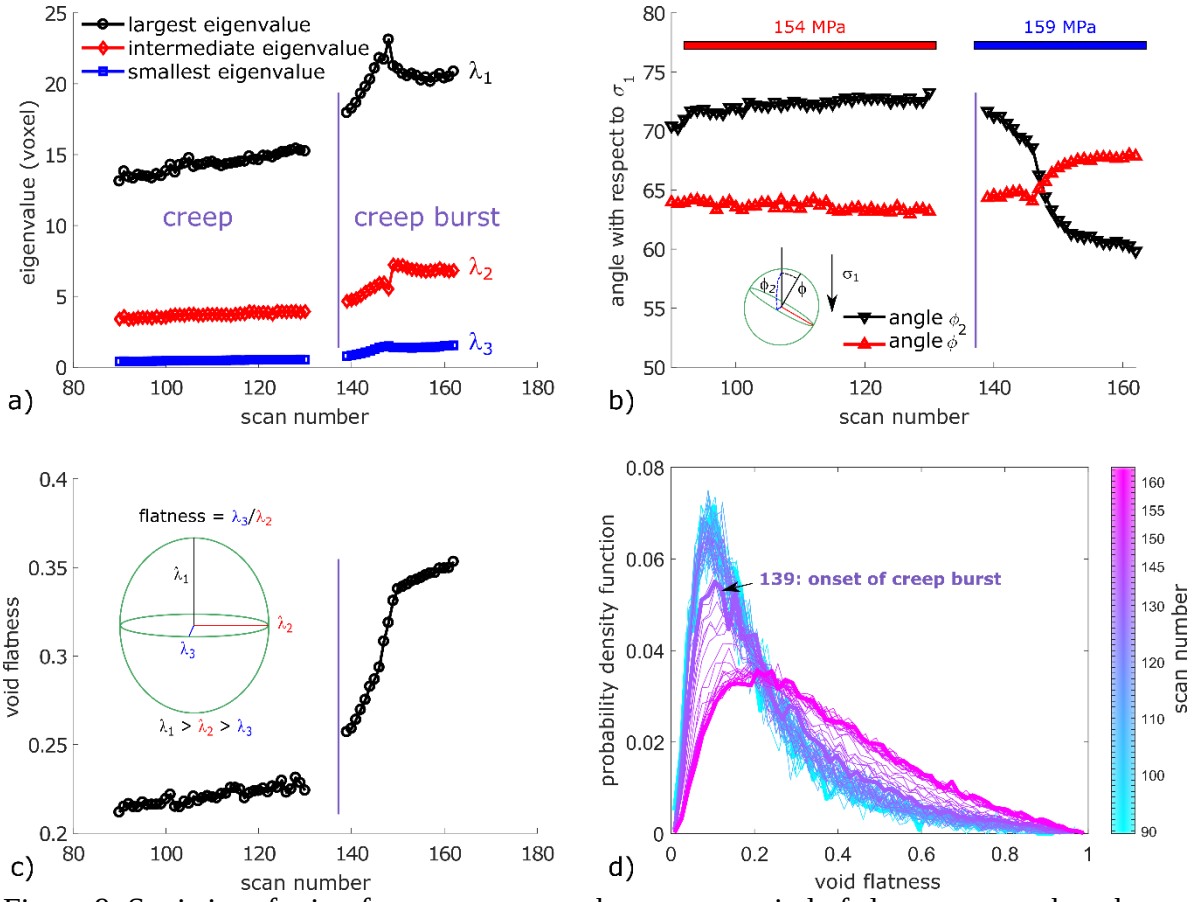

Figure 9: Statistics of microfracture geometry between a period of slower creep when the differential stress was constant and equal to 154 MPa (scans 90-130) and faster creep (i.e., creep burst) when the differential stress was constant and equal to 159 MPa (scans 139-162). a) Evolution of the average lengths of the three principle eigenvalues of the covariance matrix of all microfractures in the sample, $\lambda_1 > \lambda_2 > \lambda_3$. During the creep burst, all three values increase indicating that microfractures grow along each dimension. b) Evolution of the average angles ϕ and ϕ_2 between the horizontal axis and λ_1 and λ_3, respectively. The evolution of the angle ϕ_2 during the creep burst indicates that the smallest axis of the microfractures become oriented at an angle of 60° with respect to σ_1, indicating that the microfractures' planes tend to become oriented at 30°, a direction more favourable for shear slip. c) The average flatness of the fractures increases with deformation, indicative of crack opening. A small value of flatness, defined as the ratio between the smallest and intermediate eigenvalues, indicates a flat, penny-shaped object. The inset shows a microfracture, approximated by an ellipsoid and the three eigenvalues of the covariance matrix, which correspond to the three main axes of the ellipse. d) Evolution of the probability density function of the flatness. The mean flatness increases with time, indicative of crack opening. Scan number 139 corresponds to the onset the creep burst, where the flatness starts increasing.

3.3 Local strain accumulation

Digital volume correlation analysis characterizes the incremental volumetric and shear strains during creep deformation. In sample M83 (dry), the highest magnitudes of the

incremental local strain (>95th percentile) occurred pervasively in the volume and did not become localized until scan 141. In particular, between scans 90-140, high magnitudes of dilation and shear strain concentrated in the lower half of the sample (Figure 10a). During this period, the number of microfractures increased but the total volume of fractures did not increase significantly (Figure 8a). As the fault network nucleated, a band of high magnitudes of dilation, and a more localized zone of shear strain, formed in the upper part of the sample (Figure 10a, between scans 139-141, Movie S3). Then, larger volumes of high dilation and shear strain developed along the system-spanning fault network between scans 145 and 149 (Figure 10b). Then, slip along the fault slowed as well as the rate of new fault propagation (Figure 8a), and the highest magnitudes of incremental deformation occurred mostly in the lower part of the sample (Figure 10c) between scans 150 and 162. This increase of incremental shear strain (i.e. creep burst) corresponds to the development of the sample-spanning fault network (Figure 6) and the increase of porosity in the fault zone (Figure 7b) At the same time, the number of microfractures increased as well as their volume (Figure 8), The mean distance between microfracture centroids increased as well, indicative of a global dilation in the fault zone. Once the fault locked, after scan 150, the porosity continued to increase, mainly in the lower part of the sample (Figure 7b).

To characterize the accumulation of incremental strain in the sample, we calculate the evolution of the cumulative values of dilation, compaction, and curl. First, we sum all these values in each DVC calculation. Then, we sum cumulatively between successive scans. This procedure allows comparing the DVC results with porosity evolution. This cumulative sum over time of dilation and shear increments show a similar evolution (Figure 11). From scans 90 to 141, the cumulative dilation increases in the sample, while the shear strain magnitudes remain low. Then the cumulative dilation increases, as well as compaction and shear strain between scans 141 to 145, concurrent with the porosity increase in the sample. From scans 145 to 149, both dilation and shear strain accelerates, corresponding to the growth and slip on the sample-spanning fault. After scan 150, slip on the fault decreases and both cumulative volumetric and shear strain continue to increase at a smaller rate in the lower part of the sample (Figure 10c).

These data show that the acceleration of macroscopic creep observed between scans 141 and 150 occurred by 1) dilation of the sample along a nascent shear zone, 2) propagation of this shear zone as a quasi-planar structure that crossed the sample and slipped, 3) the slowing of slip on this fault network, slowing of the rate of fracture nucleation and diffuse deformation in the rock volume around it. This microscopic evolution characterizes the macroscopic creep bursts observed in the local strain data (Figure 3b).

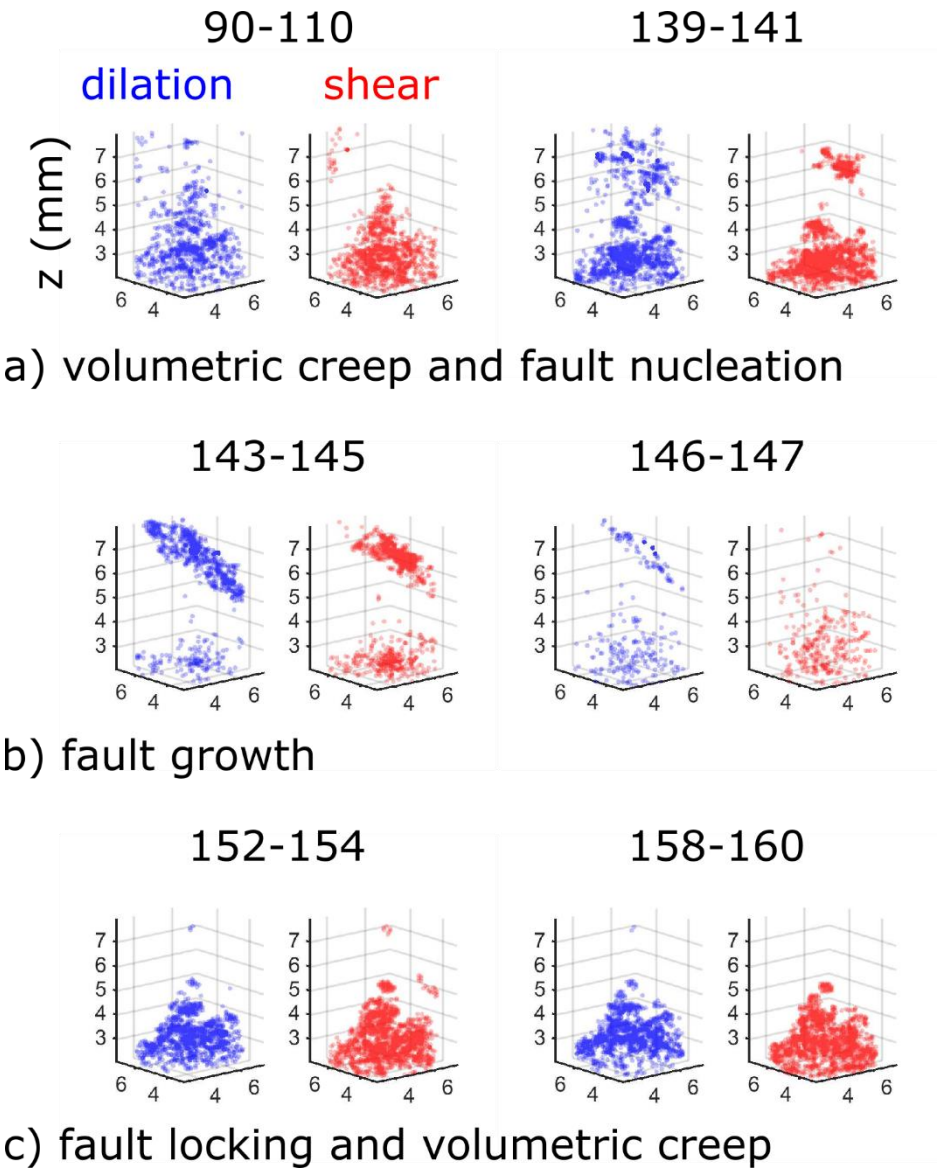

Figure 10: Local incremental strains calculated between pairs of tomograms acquired of sample M83. The numbers above each plot indicate the pair of tomograms used for the calculation. Distance units are given in mm. Colored circles show the highest 95th percentile of the incremental positive divergence (dilation, blue) and absolute value of curl (shear, red). a) Before fault network nucleation, high magnitudes of dilation and shear strain develop at the bottom of the sample. At the onset of fault network nucleation, high magnitudes of dilation and shear begin to concentrate in the top part of the sample. b) During fault network propagation across the sample, dilation dominates the volume of the future fault plane, while the high magnitudes of shear are confined to a smaller volume. c) After some time, the fault locks, accommodating lower magnitudes of strain (<95th percentile), and volumetric deformation at the bottom of the sample accommodates creep. The Figures 3b and 6 show the axial strain and 3D views of the sample. The Movie S3 shows the complete evolution of the incremental dilation, contraction, and shear strain.

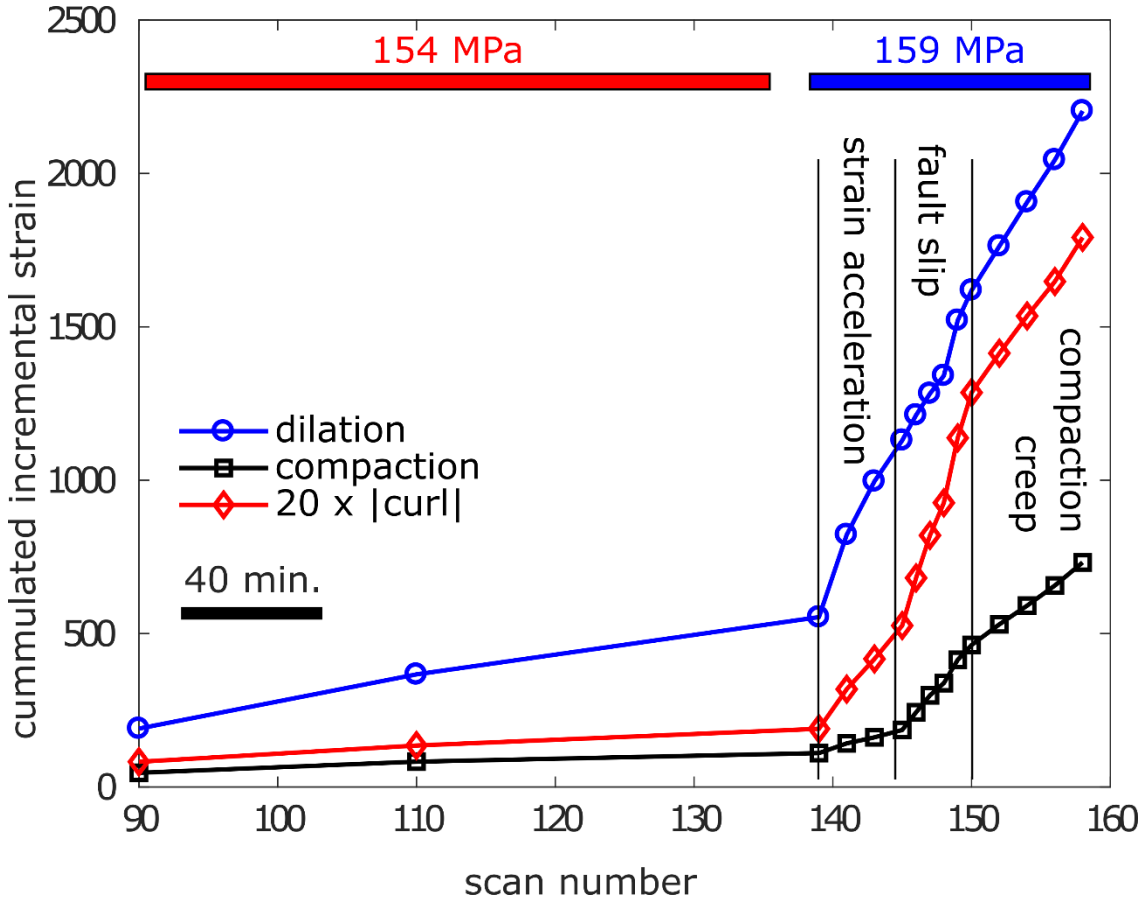

Figure 11: Cumulative strain evolution at constant differential stress conditions (154 or 159 MPa) in sample M83 before, during and after the creep burst. The black bar indicates the time scale. The black vertical lines mark the onset of the acceleration of dilation, compaction, and shear (the onset of the creep burst at scan 139), the onset of fault nucleation and slip, and the period where strain was accommodated by volumetric compaction creep in the lower part of the sample and not only localized along the fault.

4 Discussion

4.1 Creep in Carrara marble

Our experimental results share similarities with previous experiments of brittle creep in Carrara marble. At high temperature, above 400°C, several mechanisms produce creep of Carrara marble including the formation of twins, grain boundary sliding and activation of dislocation displacements (e.g., Quintanilla-Terminel and Evans, 2016). However, at lower temperature, the creep mechanism in marble is mainly due to the growth and coalescence of microfractures (Tal et al., 2016). Triaxial creep experiments with cyclic loading on marble at room temperature have shown that the macroscopic axial strain increases with time with a slightly nonlinear trend, under a differential stress loading equal to 60% of the short term strength of the material (Figure 7 in Yang et al., 2015). Two different viscous dissipation processes were proposed by these authors that could produce this nonlinearity: a visco-elastic

term with an exponential dependence in time and a visco-plastic term with a linear dependence in time.

Below 50% of the differential stress at macroscopic failure, creep in marble was below the detection limit of triaxial compression laboratory experiments (Liu et al., 2017). At room temperature, 30 MPa confining pressure and 150 MPa differential stress, the creep rate of Jinping Bed marble in China was close to 10^{-7} s^{-1} (Liu et al., 2017). For other marble samples from the same area, the creep strain rate measured at 35 MPa confining pressure, 145 MPa differential stress, and room temperature, was smaller, around $2 \cdot 10^{-8}$ s^{-1} (Yang et al., 2015). In our experiments, the steady state creep rate before the creep burst is in the range $6.2 \cdot 10^{-7}$-$5.0 \cdot 10^{-5}$ s^{-1} under constant differential stress and room temperature (Figure 3a). These values are slightly higher than those reported by Yang et al. (2015) and Liu et al (2017), probably because our creep rates are measured at a differential stress closer to failure than in their experiments. However, the main difference is that we observed creep bursts in our data, with strain rates in the range $2.5 \cdot 10^{-5}$-$6.4 \cdot 10^{-4}$ s^{-1} (Figure 3b), several orders of magnitude larger than creep rates previously reported in marble (e.g., Yang et al., 2015; Liu et al., 2017).

4.2 Brittle creep and faulting in rock experiments

Other laboratory experiments performed on crystalline low porosity rocks have measured strain rates during brittle creep. Lockner (1993) deformed granite samples at room temperature, under constant confining and pore pressure conditions, as the axial stress was cycled to enhance creep. Macroscopic axial strain increases with a linear dependence of time when the applied differential stress is at some distance (80%) of the failure stress, i.e., secondary creep (Figure 1). This secondary creep strain rate follows an exponential dependence with the applied (constant) stress (Lockner, 1993). From the recording of acoustic emissions and post-mortem observations of microfractures, the nucleation and subcritical growth of microfractures have been identified as dominant microstructural mechanisms that accumulate irreversible strain (Lockner, 1993; Ross et al., 1983; Scholz, 1968). In our experiments, steady state creep occurs under a differential stress of 154 MPa in sample M83 (scans 90-130) and coincides in time with the nucleation and growth of microfractures (Figures 3a, 5). During this deformation stage, the porosity increases slightly (Figure 3a). The average shape of microfracture remains similar, and their orientation is consistently near parallel to σ_1 with an angle ϕ_2 close to 70° (Figure 9). These dilatant vertical cracks formed in the sample produce irreversible damage. With continuing creep, when approaching fault formation, these microfractures coalesced to form a fault network that extended across the sample. These stages of fracture coalescence were also observed in 2D experiments on Carrara marble (Tal et al., 2016).

In a series of experiments on crystalline rock performed under constant differential stress, Lei et al. (2000) measured a non-linear increase of the rate of acoustic emissions that occurred within one minute in a rock sample loaded near failure. The spatial distribution of the acoustic emissions indicates that they were initially distributed throughout the rock and then concentrated in a quasi-planar structure that evolved into a more localized fault. The zone with tensile fracturing located in front of the propagating fault, identified from acoustic emission recording, supports the existence of a dilatant process zone. The fault then propagates within this process zone, a mechanism proposed in Reches and Lockner (1994). In porous rocks, such as sandstone, acoustic emission recording show that creep remains diffuse in the volume, without localizing into a sub-planar structure (Heap et al., 2009). In the creep burst reported in the present study,

strain localization occurs initially in the formation of a dilatant (high porosity) zone in the middle of the sample (Figures 6 and 10, scans 143-145), with low magnitudes of cumulative shear strain (Figure 11), and higher local porosity increase. Then high magnitudes of shear strain localized into a system-spanning fault (scans 143-147 in Figure 10). After the fault network crossed the sample, slip along it decreased, the rate of fracture propagation slowed, and creep continued in the lower half of the core (Figures 7b, 8, 10c, scans 150-162).

The development of faults in laboratory creep experiments has been observed in granite (Lei et al., 2000) and basalt (Heap et al., 2011). In amphibolite (Satoh et al., 1996), a fault developed along a pre-existing joint that acted as a nucleation site for localized deformation. In these experiments on granite, basalt and amphibolite, an increase of the number and the energy of acoustic emissions occurred when approaching failure. This increase was interpreted as the development of microfractures at the grain scale. In experiment M83 (dry), we directly observe that fault growth occurs slowly, with varying rates of creep, rather than a faster evolution toward catastrophic failure. Moreover, once the fault network spans the system, slip on it decreased, and creep deformation was accommodated in the lower part of the sample by the opening of new microfractures, rather than through accelerating slip along this through-going fault network. Conversely, in sample M84 (wet), the creep burst precedes macroscopic failure, and occurred during the tertiary creep phase.

An important difference between our two experiments is that the macroscopic strain rate during the creep burst is around 25 times faster in sample M83 (wet) (Figure 3b), than for sample M84 (dry) (Figure 4). The influence of water on accelerated creep has also been observed in granite (Krantz, 1982), sandstone (Baud et al., 2000), and single calcite crystals (Røyne et al., 2011). The presence of water lowers the surface energy between calcite and water during fracture propagation, producing the faster rate of fracture growth, as observed in sample M84.

5 Conclusions

The experiments reported in the present study indicate that, under constant stress conditions at room temperature, cores of Carrara marble deform macroscopically in creep due mainly to the growth of microfractures. Both secondary and tertiary creep occur in the experiments (Figure 1). The stage of tertiary creep includes creep bursts: transient accelerations of creep, similar to slow slip events measured on continental faults that have been interpreted as an acceleration of slip along a pre-existing fault plane (Linde et al., 1996; Jolivet et al., 2013; 2015, Rousset et al., 2016). In our experiment, the creep bursts did not occur on a pre-existing fault, but coincided with the development of a system-spanning connected fault network. At the microscale, the creep burst coincides in time with the 1) localization of fractures along a quasi-planar structure, 2) increase of the aperture of the microfractures, 3) rotation of the orientation of the microfractures to 30° to σ_1, more favorable for shear deformation, and 4) localization of the highest magnitudes of the local dilation and shear strain into a sub-planar inclined structure. Once formed, slip on the fault network decreased, the high magnitudes of strain delocalized from this fault zone, the rate of fault propagation slowed, and creep continued in the volume around the fault. Our results therefore demonstrate that creep bursts in laboratory experiments may indicate the birth of a new fault, and not only an acceleration of transient slip on a pre-existing fault which is the common explanation for slow slip events observed in active faults.

Acknowledgments and Data

We thank Elodie Boller, Paul Tafforeau, and Alexander Rack for providing advice on the design of the tomography setup, and Sanchez Technology for building the deformation apparatus. The authors received funding from the Norwegian Research Council (grant 272217). X-ray tomography data of the two experiments will be available on Norstore (https://archive.norstore.no/) at the time of publication of the present study.

References

Amitrano, D., & Helmstetter, A. (2006), Brittle creep, damage, and time to failure in rocks, *Journal of Geophysical Research*, 111, B11201, doi:10.1029/2005JB004252.

Anderson, E. M. (1905), The dynamics of faulting. *Transactions of the Edinburgh Geological Society*, 8(3), 387-402.

Aslan, G., Lasserre, C., Cakir, Z., Ergintav, S., Özarpaci, S., Dogan, U., Bilham, R., & Renard, F. (2019), Shallow creep along the 1999 Izmit Earthquake rupture (Turkey) from GPS and high temporal resolution interferometric synthetic aperture radar data (2011–2017). *Journal of Geophysical Research: Solid Earth*, 124(2), 2218-2236.

Baud, P., Zhu, W., & Wong, T.-F. (2000), Failure mode and weakening effect of water on sandstone. *Journal of Geophysical Research*, 105 (B7), 16371-16389. doi:10.1029/2000JB900087.

Baud, P., & Meredith, P. G. (1997), Damage accumulation during triaxial creep of Darley Dale sandstone from pore volumometry and acoustic emission. *International Journal of Rock Mechanics and Mining Sciences*, 34(3-4), 24-e1.

Bouchon, M., Karabulut, H., Aktar, M., Özalaybey, S., Schmittbuhl, J., & Bouin, M. P. (2011), Extended nucleation of the 1999 Mw 7.6 Izmit earthquake, *Science*, 331(6019), 877-880.

Brace, W. F., Paulding Jr., B. W., & Scholz, C. H. (1966), Dilatancy in the fracture of crystalline rocks, *Journal of Geophysical Research*, 71, 3939–3953.

Brantut, N., Heap, M. J., Meredith, P. G., & Baud, P. (2013), Time-dependent cracking and brittle creep in crustal rocks: A review. *Journal of Structural Geology*, 52, 17-43.

Buades, A., Coll, B., & Morel, J. M. (2005), A non-local algorithm for image denoising. In Computer Society Conference on Computer Vision and Pattern Recognition, 2005, IEEE vol. 2, pp. 60-65.

Bürgmann, R. (2018), The geophysics, geology and mechanics of slow fault slip. *Earth and Planetary Science Letters*, 495, 112-134.

Carlà, T., Intrieri, E., Raspini, F., Bardi, F., Farina, P., Ferretti, A., Colombo, D., Novali, F., & Casagli, N. (2019), Perspectives on the prediction of catastrophic slope failures from satellite InSAR. *Scientific Reports*, 9(1), 1-9.

Cox, S. J. D., & Scholz, C. H. (1988), Rupture initiation in shear fracture of rocks: an experimental study. *Journal of Geophysical Research: Solid Earth*, 93(B4), 3307-3320.

643 French, M. E., & Zhu, W. (2017), Slow fault propagation in serpentinite under conditions of high
644 pore fluid pressure. *Earth and Planetary Science Letters*, 473, 131-140.

645 Gratier, J. P., Dysthe, D. K., & Renard, F. (2013), The role of pressure solution creep in the
646 ductility of the Earth's upper crust. In *Advances in Geophysics* (Vol. 54, pp. 47-179).
647 Elsevier.

648 Griggs, D. (1939), Creep of rocks. *The Journal of Geology*, 47(3), 225-251.

649 Griffith, W. A., Nielsen, S., Di Toro, G., & Smith, S. A. F. (2010), Rough faults, distributed
650 weakening, and off-fault deformation, *Journal of Geophysical Research*, 115, B08409,
651 doi:10.1029/2009JB006925.

652 Guglielmi, Y., Cappa, F., Avouac, J. P., Henry, P., & Elsworth, D. (2015), Seismicity triggered
653 by fluid injection–induced aseismic slip. *Science*, 348(6240), 1224-1226.

654 Handwerger, A. L., Huang, M. H., Fielding, E. J., Booth, A. M., & Bürgmann, R. (2019), A shift
655 from drought to extreme rainfall drives a stable landslide to catastrophic failure. *Scientific*
656 *Reports*, 9(1), 1-12.

657 Heap, M. J., Baud, P., Meredith, P. G., Bell, A. F., & Main, I. G. (2009), Time-dependent brittle
658 creep in Darley Dale sandstone, *Journal of Geophysical Research*, 114, B07203,
659 doi:10.1029/2008JB006212.

660 Heap, M. J., Baud, P., Meredith, P. G., Vinciguerra, S., Bell, A. F., & Main, I. G. (2011), Brittle
661 creep in basalt and its application to time-dependent volcano deformation. *Earth and*
662 *Planetary Science Letters*, 307(1-2), 71-82.

663 Jolivet, R., Lasserre, C., Doin, M. P., Peltzer, G., Avouac, J. P., Sun, J., & Dailu, R. (2013),
664 Spatio-temporal evolution of aseismic slip along the Haiyuan fault, China: Implications
665 for fault frictional properties. *Earth and Planetary Science Letters*, 377, 23-33.

666 Jolivet, R., Candela, T., Lasserre, C., Renard, F., Klinger, Y., & Doin, M. P. (2015), The burst-
667 like behavior of aseismic slip on a rough fault: The creeping section of the Haiyuan fault,
668 China. *Bulletin of the Seismological Society of America*, 105(1), 480-488.

669 Kandula, N., Cordonnier, B., Boller, E., Weiss, J., Dysthe, D. K., & Renard, F. (2019), Dynamics
670 of microscale precursors during brittle compressive failure in Carrara marble. *Journal of*
671 *Geophysical Research: Solid Earth*, 124(6), 6121-6139.

672 Kie, T. T., Quan, S. Z., Hai, Y. Z., & Yang, W. X. (1989), Dilatancy, creep and relaxation of
673 brittle rocks measured with the 8000 kN multipurpose triaxial apparatus. *Physics of the*
674 *Earth and Planetary Interiors*, 55(3-4), 335-352.

675 Kranz, R. L., & Scholz, C. H. (1977), Critical dilatant volume of rocks at the onset of tertiary
676 creep. *Journal of Geophysical Research*, 82(30), 4893-4898.

677 Kranz, R. L. (1980), The effects of confining pressure and stress difference on static fatigue of
678 granite. *Journal of Geophysical Research: Solid Earth*, 85(B4), 1854-1866.

679 Kranz, R.L., Harris, W.J., & Carter, N.L. (1982), Static fatigue of granite at 200 °C. *Geophysical*
680 *Research Letters*, 9 (1), 1-4. doi:10.1029/GL009i001p00001.

681 Linde, A. T., Gladwin, M. T., Johnston, M. J., Gwyther, R. L., & Bilham, R. G. (1996), A slow
682 earthquake sequence on the San Andreas fault. *Nature*, 383(6595), 65-68.

683 Liu, Z., & Shao, J. (2017), Strength behavior, creep failure and permeability change of a tight
684 marble under triaxial compression. *Rock Mechanics and Rock Engineering*, 50(3), 529-
685 541.

686 Lockner, D., & Byerlee, J. (1977), Acoustic emission and creep in rock at high confining
687 pressure and differential stress. *Bulletin of the Seismological Society of America*, 67(2),
688 247-258.

689 Lockner, D. (1993). Room temperature creep in saturated granite, *Journal of Geophysical*
690 *Research*, 98(B1), 475– 487, doi:10.1029/92JB01828.

691 Lohman, R. B., & McGuire, J. J. (2007), Earthquake swarms driven by aseismic creep in the
692 Salton Trough, California. *Journal of Geophysical Research: Solid Earth*, 112(B4).

693 Lomnitz, C. (1956), Creep measurements in igneous rocks. *The Journal of Geology*, 64(5), 473-
694 479.

695 Main, I. G. (1999), Applicability of time-to-failure analysis to accelerated strain before
696 earthquakes and volcanic eruptions. *Geophysical Journal International*, 139(3), F1-F6.
697 doi:10.1046/j.1365-246x.1999.00004.x.

698 Main, I. G. (2000), A damage mechanics model for power-law creep and earthquake aftershock
699 and foreshock sequences. *Geophysical Journal International*, 142(1), 151-161.

700 McBeck, J., Kobchenko, M., Hall, S. A., Tudisco, E., Cordonnier, B., Meakin, P., & Renard, F.,
701 (2018), Investigating the onset of strain localization within anisotropic shale using digital
702 volume correlation of time-resolved X-ray microtomography images. *Journal of*
703 *Geophysical Research: Solid Earth*, doi:10.1029/2018JB015676.

704 Mirone, A., Brun, E., Gouillart, E., Tafforeau, P., & Kieffer, J. (2014), The PyHST2 hybrid
705 distributed code for high speed tomographic reconstruction with iterative reconstruction
706 and a priori knowledge capabilities. *Nuclear Instruments and Methods in Physics*
707 *Research Section B: Beam Interactions with Materials and Atoms*, 324, 41-48.
708 doi:10.1016/j.nimb.2013.09.030.

709 Ngwenya, B. T., Main, I. G., Elphick, S. C., Crawford, B. R., & Smart, B. G. (2001), A
710 constitutive law for low-temperature creep of water-saturated sandstones. *Journal of*
711 *Geophysical Research: Solid Earth*, 106(B10), 21811-21826.

712 Peng, S., & Johnson, A. M. (1972), Crack growth and faulting in cylindrical specimens of
713 Chelmsford granite. *International Journal of Rock Mechanics and Mining Science*, 9, 37-
714 86.

715 Quintanilla-Terminel, A., & Evans, B. (2016), Heterogeneity of inelastic strain during creep of
716 Carrara marble: Microscale strain measurement technique. *Journal of Geophysical*
717 *Research: Solid Earth*, 121(8), 5736-5760.

718 Reches, Z., & Lockner, D. A. (1994), Nucleation and growth of faults in brittle rocks, *Journal of*
719 *Geophysical Research*, 99, 18159-18173.

720 Renard, F., Cordonnier, B., Dysthe, D. K., Boller, E., Tafforeau, P., & Rack, A. (2016), A
721 deformation rig for synchrotron microtomography studies of geomaterials under
722 conditions down to 10 km depth in the Earth. *Journal of Synchrotron Radiation*, 23(4),
723 1030-1034.

Renard, F., Cordonnier, B., Kobchenko, M., Kandula, N., Weiss, J., & Zhu, W. (2017), Microscale characterization of rupture nucleation unravels precursors to faulting in rocks. *Earth and Planetary Science Letters*, 476, 69-78.

Renard, F., McBeck, J., Kandula, N., Cordonnier, B., Meakin, P., & Ben-Zion, Y. (2019), Volumetric and shear processes in crystalline rock approaching faulting, *Proceedings of the National Academy of Sciences*, 116, 16234-16239, doi: 10.1073/pnas.1902994116.

Ross, J. V., Bauer, S. J., & Carter, N. L. (1983), Effect of the α-β quartz transition on the creep properties of quartzite and granite. *Geophysical Research Letters*, 10(12), 1129-1132.

Røyne, A., Bisschop, J., & Dysthe, D. K. (2011), Experimental investigation of surface energy and subcritical crack growth in calcite, *Journal of Geophysical Research*, 116, B04204, doi:10.1029/2010JB008033.

Rutter, E. H. (1976), A discussion on natural strain and geological structure-the kinetics of rock deformation by pressure solution. *Philosophical Transactions of the Royal Society of London. Series A, Mathematical and Physical Sciences*, 283(1312), 203-219.

Satoh, T., Shivakumar, K., Nishizawa, O., & Kusunose, K. (1996), Precursory localization and development of microfractures along the ultimate fracture plane in amphibolite under triaxial creep. *Geophysical Research Letters*, 23(8), 865-868.

Scholz, C. H. (1968), Mechanism of creep in brittle rock. *Journal of Geophysical Research*, 73(10), 3295-3302.

Segall, P., & Pollard, D. D. (1980), Mechanics of discontinuous faults. *Journal of Geophysical Research: Solid Earth*, 85(B8), 4337-4350.

Shengqi, Y., & Jiang, Y. (2010), Triaxial mechanical creep behavior of sandstone. *Mining Science and Technology*, 20(3), 339-349.

Tal, Y., Evans, B., & Mok, U. (2016), Direct observations of damage during unconfined brittle failure of Carrara marble. *Journal of Geophysical Research: Solid Earth*, 121(3), 1584-1609.

Tsai, L. S., Hsieh, Y. M., Weng, M. C., Huang, T. H., & Jeng, F. S. (2008), Time-dependent deformation behaviors of weak sandstones. *International Journal of Rock Mechanics and Mining Sciences*, 45(2), 144-154.

Tudisco, E., Andò, E., Cailletaud, R., & Hall, S. A. (2017), TomoWarp2: a local digital volume correlation code. *SoftwareX*, 6, 267-270.

Vermilye, J. M., & Scholz, C. H. (1999), Fault propagation and segmentation: insight from the microstructural examination of a small fault. *Journal of Structural Geology*, 21(11), 1623-1636.

Voight, B. (1989), A relation to describe rate-dependent material failure. *Science*, 243, 200–203.

Wei, S., Avouac, J. P., Hudnut, K. W., Donnellan, A., Parker, J. W., Graves, R. W., Helmberger, D., Fielding, E., Liu, Z., Cappa, F., & Eneva, M. (2015), The 2012 Brawley swarm triggered by injection-induced aseismic slip. *Earth and Planetary Science Letters*, 422, 115-125.

763 Xu, S., & Ben-Zion, Y. (2013), Numerical and theoretical analyses of in-plane dynamic rupture
764 on a frictional interface and off-fault yielding patterns at different scales. *Geophysical*
765 *Journal International*, 193(1), 304-320.

766 Yang, S. Q., Xu, P., Ranjith, P. G., Chen, G. F., & Jing, H. W. (2015), Evaluation of creep
767 mechanical behavior of deep-buried marble under triaxial cyclic loading. *Arabian*
768 *Journal of Geosciences*, 8(9), 6567-6582.

769 Zhao, Q., Tisato, N., Kovaleva, O. & Grasselli, G. (2018), Direct observation of faulting by
770 means of rotary shear tests under X-ray micro-computed tomography. *Journal of*
771 *Geophysical Research*, 123 (9), 7389-7403.

Figure 1.

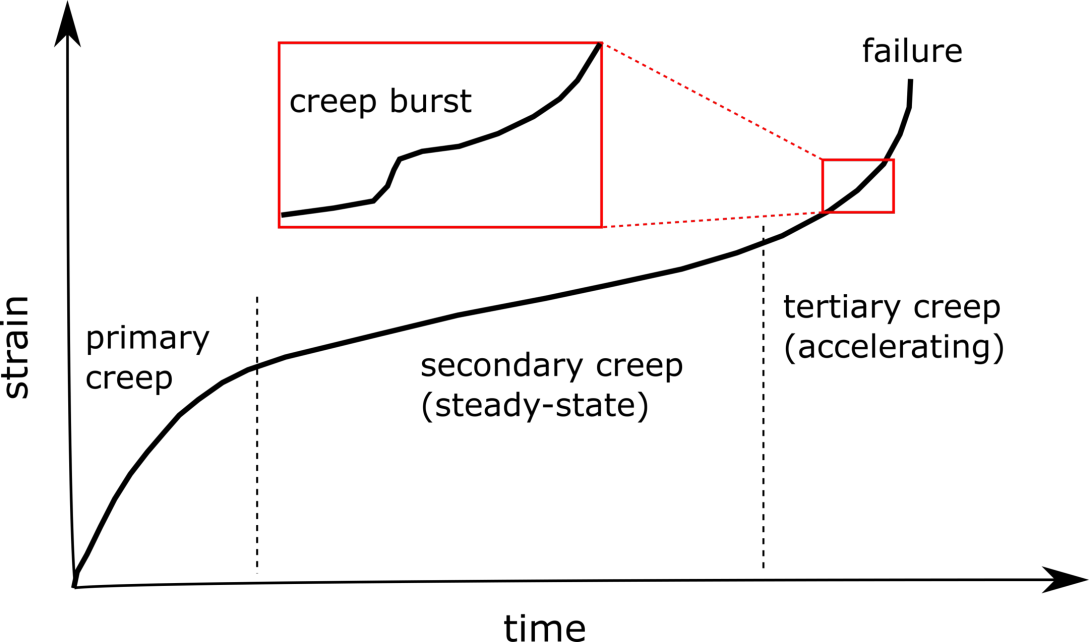
creep burst
failure
strain
primary
creep
secondary creep
(steady-state)
tertiary creep
(accelerating)
time

Figure 2.

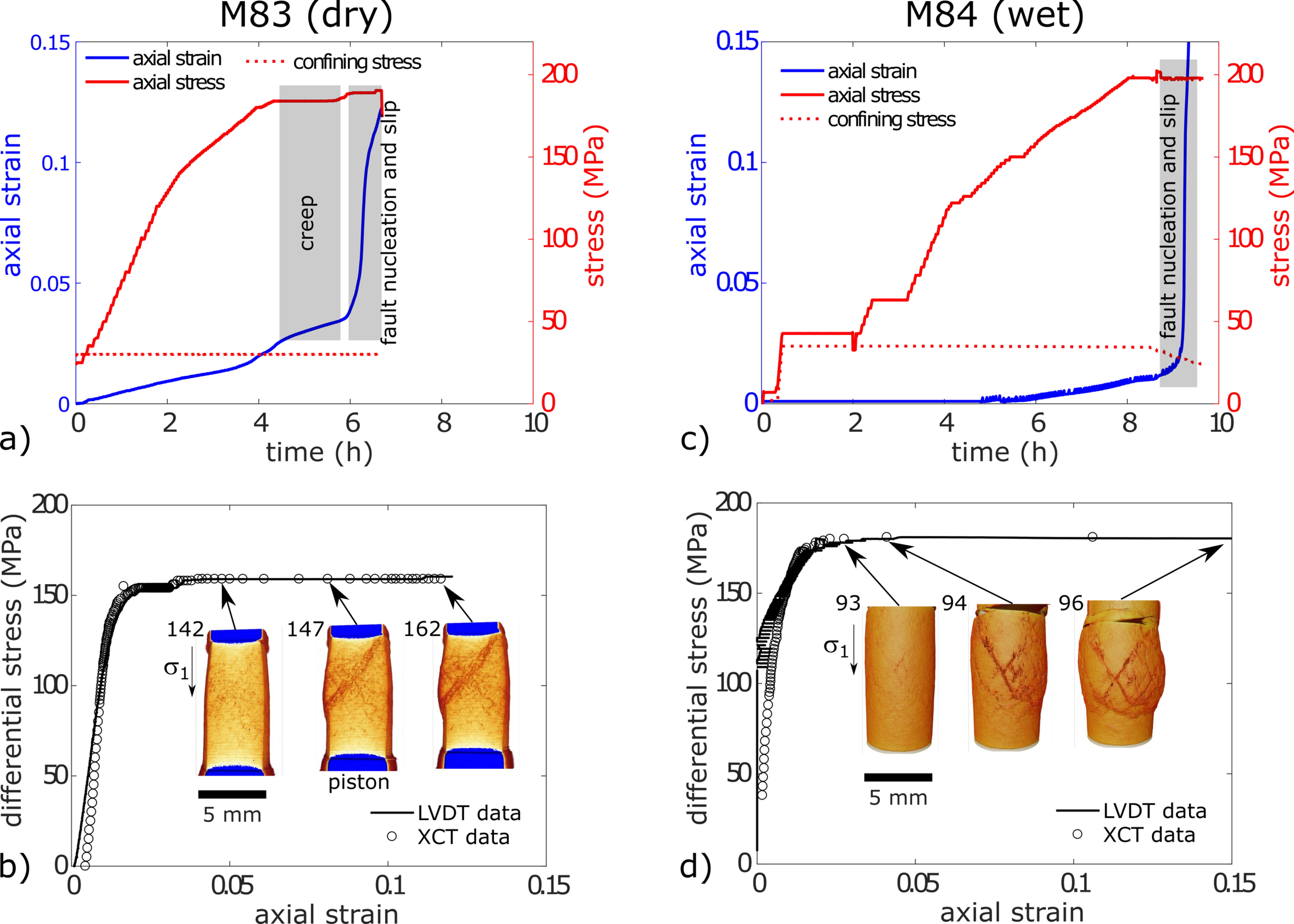
M83 (dry)
M84 (wet)
axial strain
axial stress
confining stress
creep
fault nucleation and slip
stress (MPa)
time (h)
a)
c)
differential stress (MPa)
axial strain
142
147
162
93
94
96
σ1
5 mm
piston
LVDT data
XCT data
b)
d)

Figure 3.

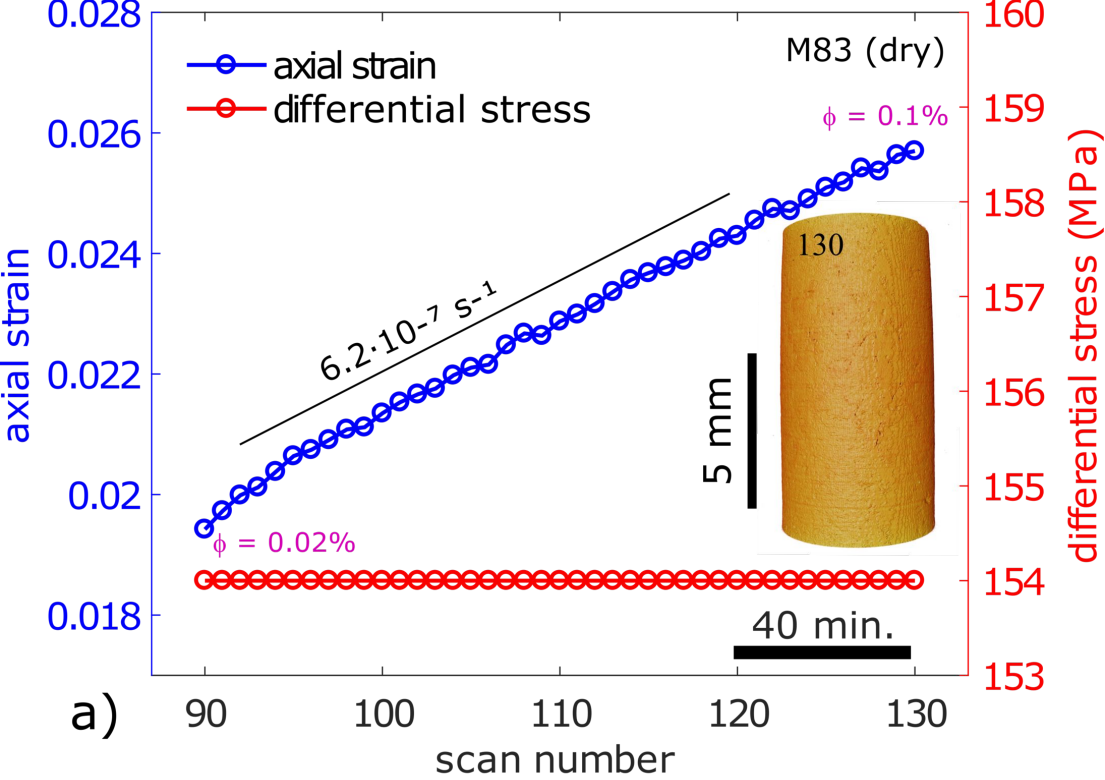
M83 (dry)
axial strain
differential stress
ϕ = 0.1%
ϕ = 0.02%
6.2·10-7 s-1
130
5 mm
40 min.
a)
scan number
axial strain
differential stress (MPa)

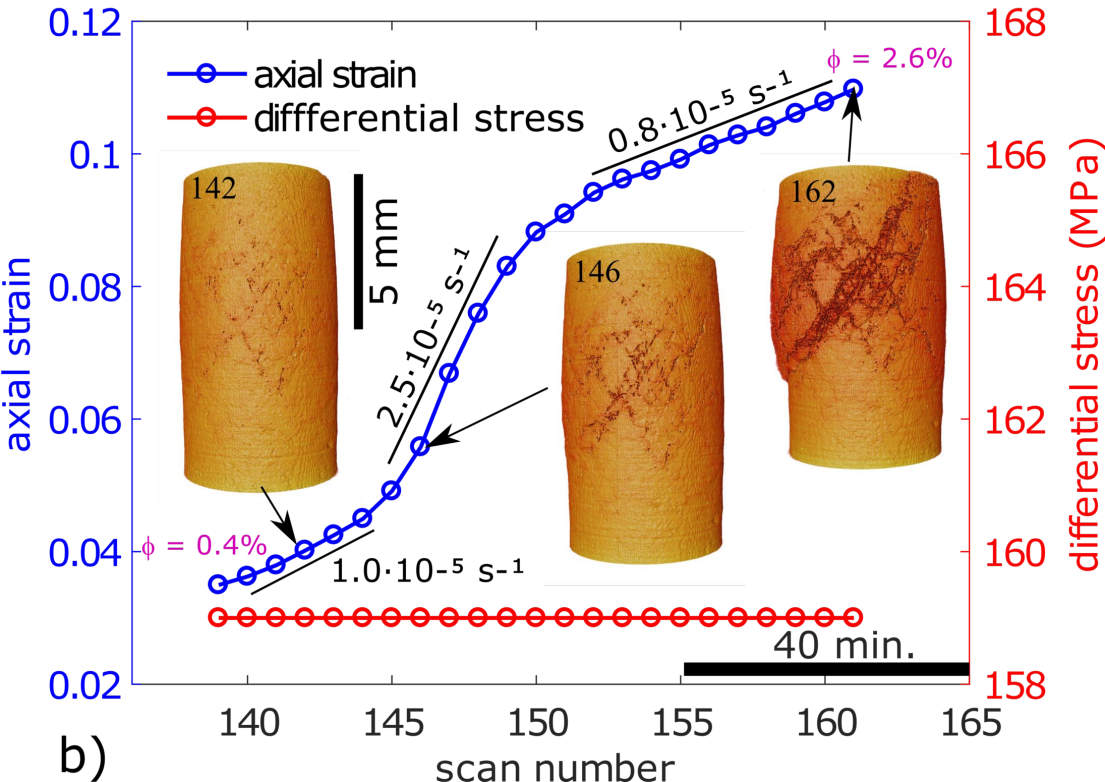
axial strain
diffferential stress
ϕ = 2.6%
ϕ = 0.4%
0.8·10-5 s-1
2.5·10-5 s-1
1.0·10-5 s-1
142
146
162
5 mm
40 min.
b)
scan number
axial strain
differential stress (MPa)

Figure 4.

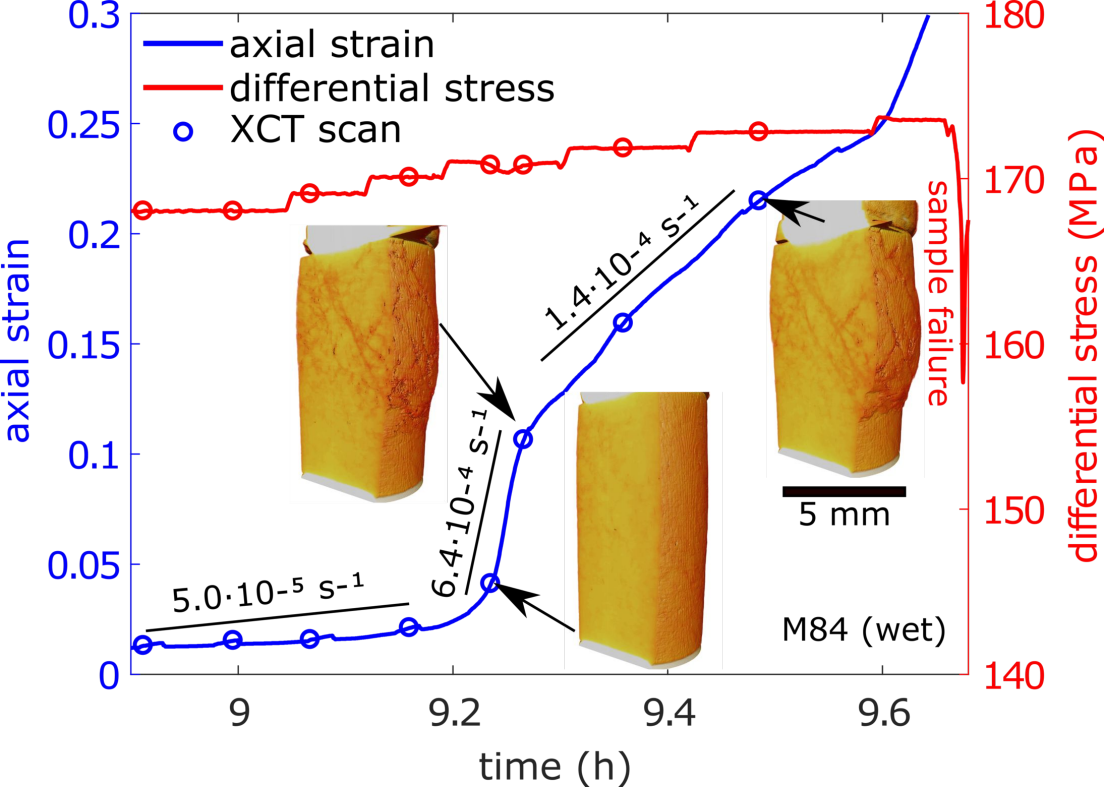
axial strain
differential stress
XCT scan
axial strain
differential stress (MPa)
time (h)
0.3
0.25
0.2
0.15
0.1
0.05
0
180
170
160
150
140
9
9.2
9.4
9.6
5.0·10-5 s-1
6.4·10-4 s-1
1.4·10-4 s-1
sample failure
5 mm
M84 (wet)

Figure 5.

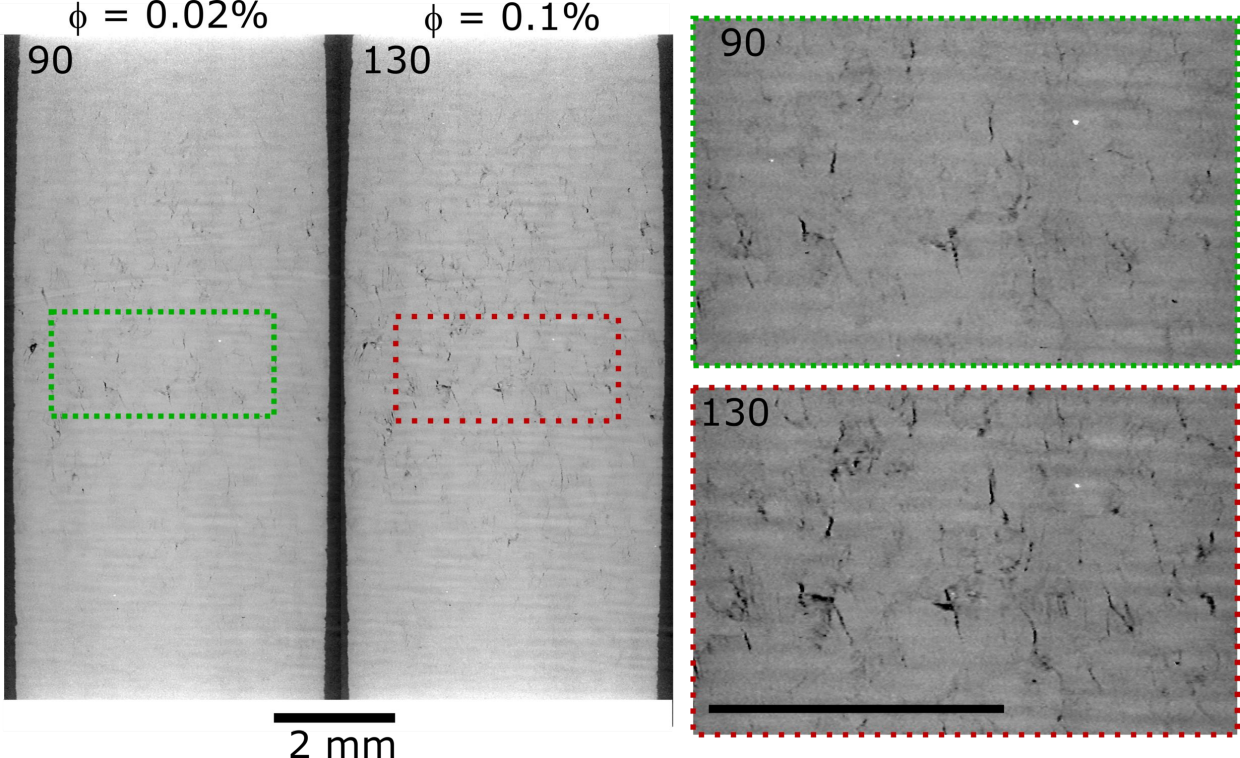
ϕ = 0.02%
ϕ = 0.1%
90
130
90
130
2 mm

Figure 6.

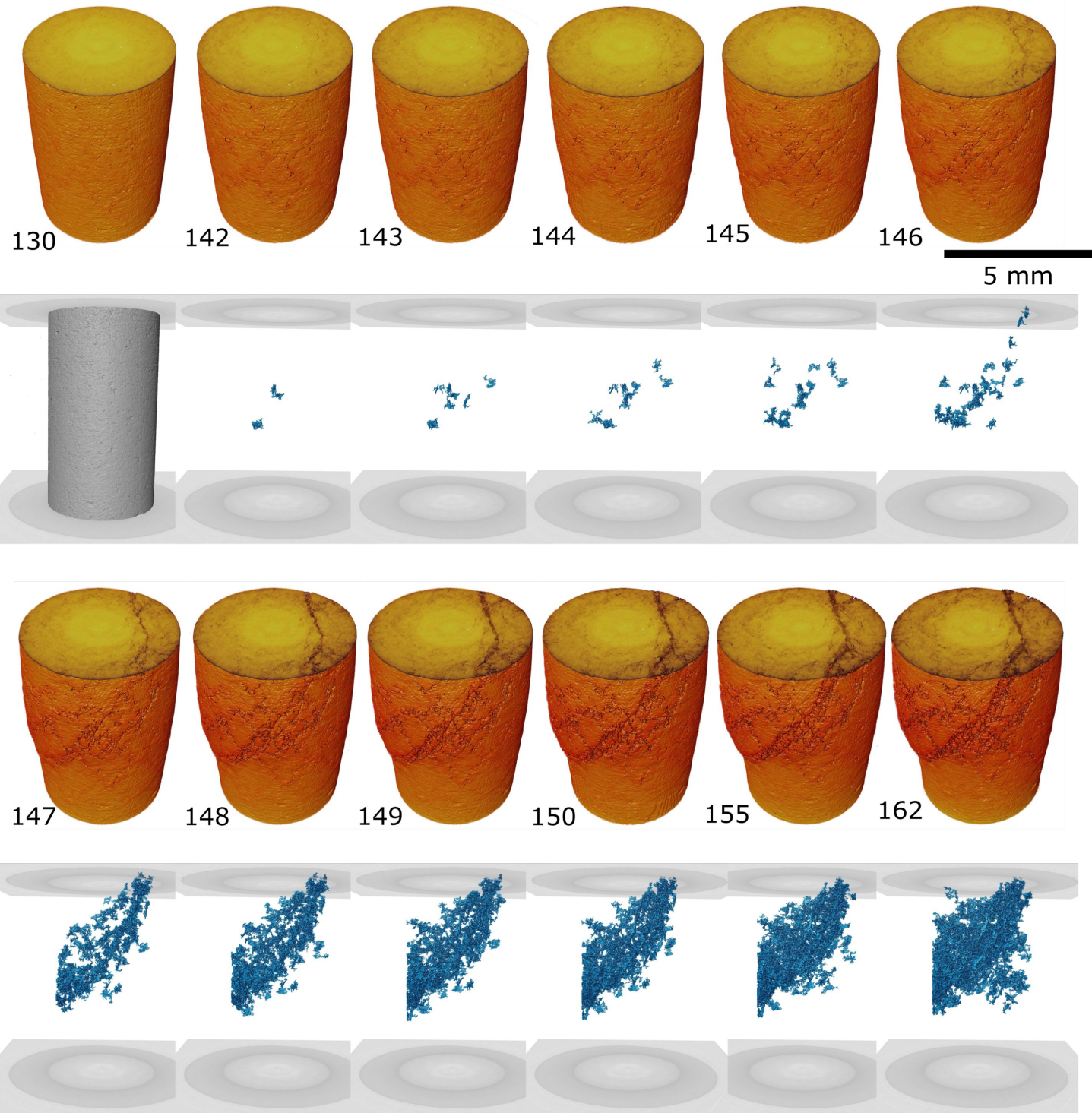
130
142
143
144
145
146
5 mm
147
148
149
150
155
162

Figure 7.

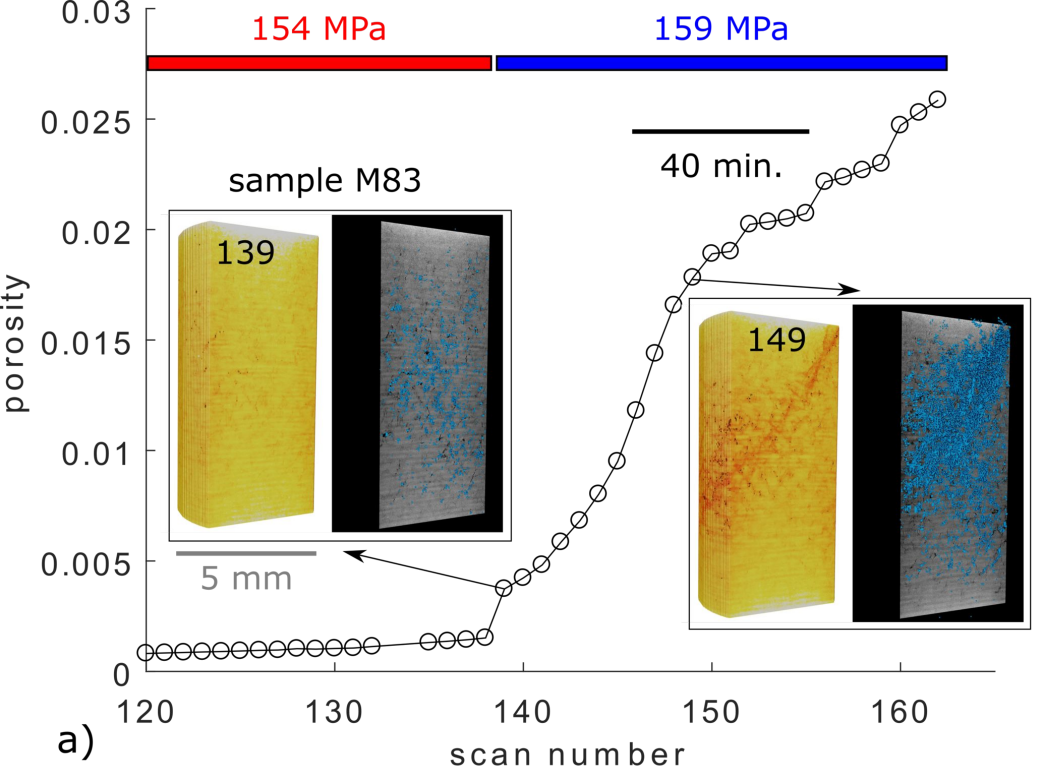
154 MPa
159 MPa
40 min.
sample M83
139
149
5 mm
porosity
scan number
a)

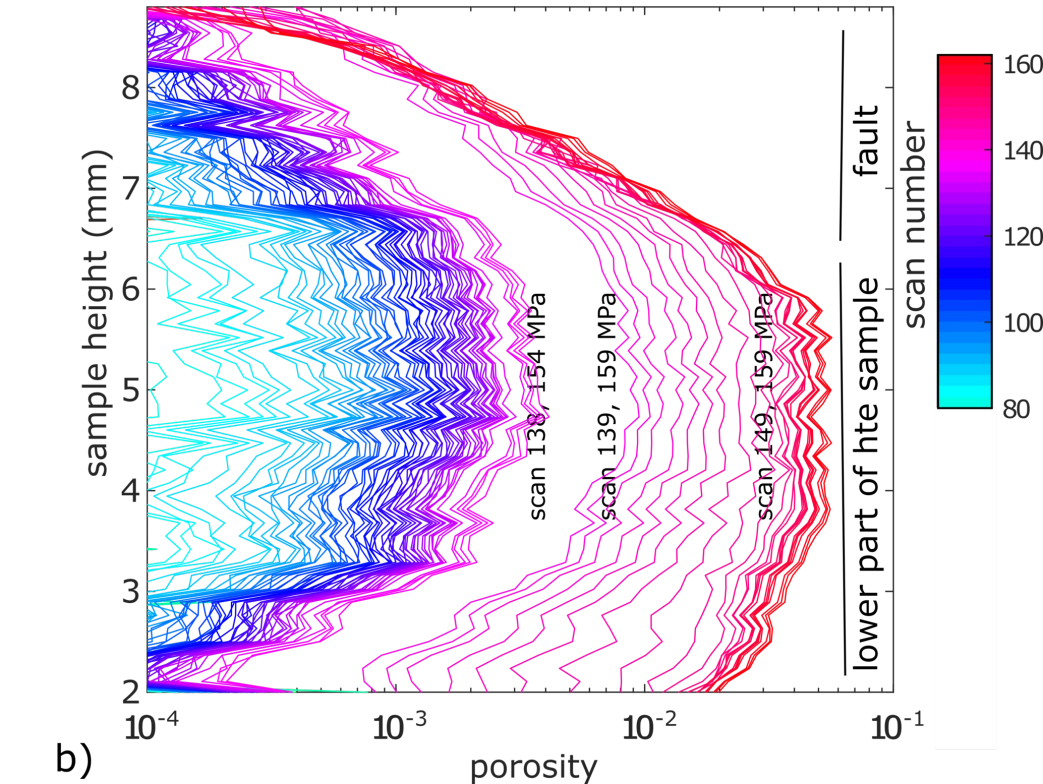
sample height (mm)
porosity
scan number
fault
lower part of hte sample
scan 139, 154 MPa
scan 139, 159 MPa
scan 149, 159 MPa
b)

Figure 8.

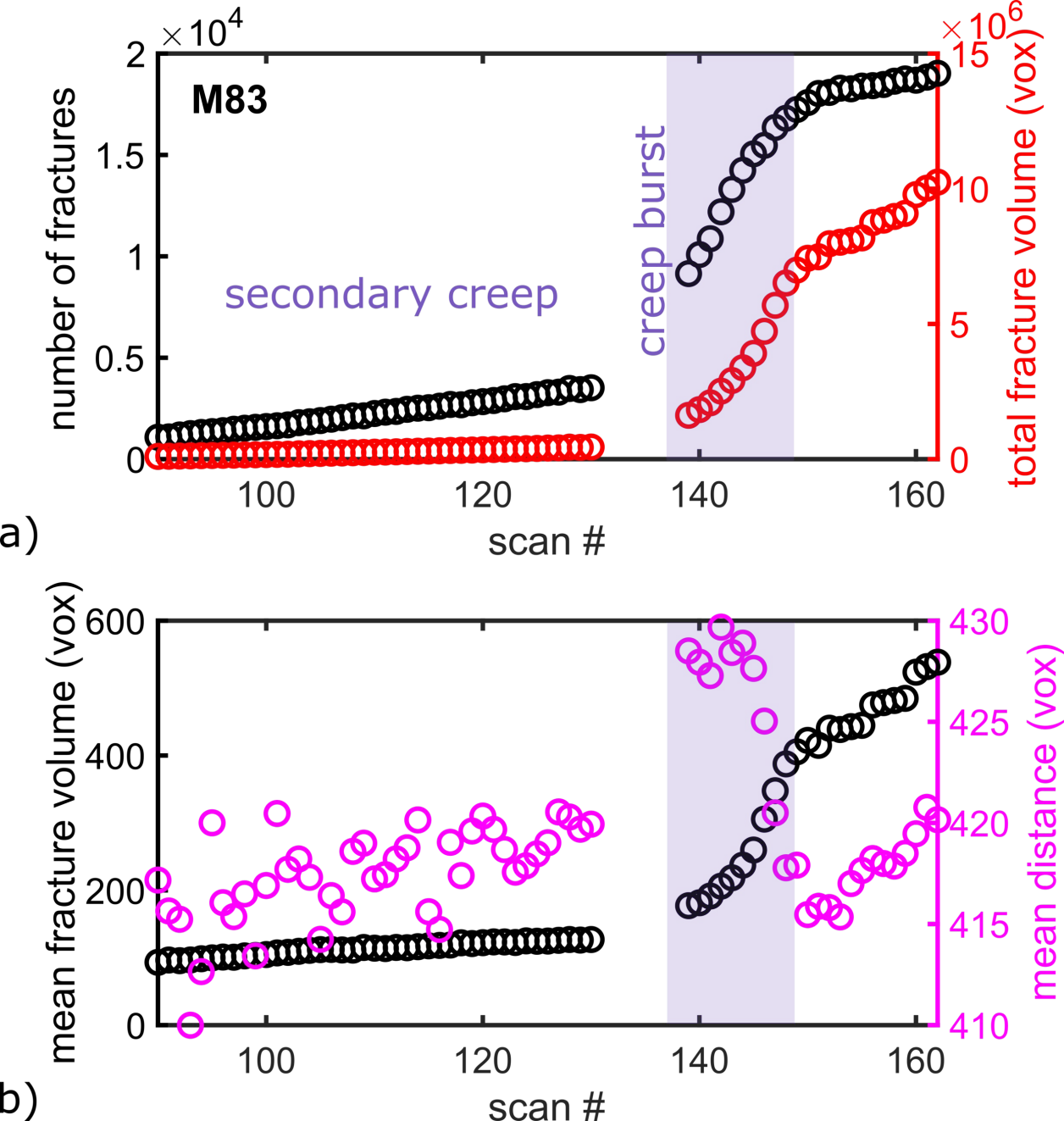
M83
secondary creep
creep burst
number of fractures
×10^4
total fracture volume (vox)
×10^6
scan #
a)
mean fracture volume (vox)
mean distance (vox)
scan #
b)

Figure 9.

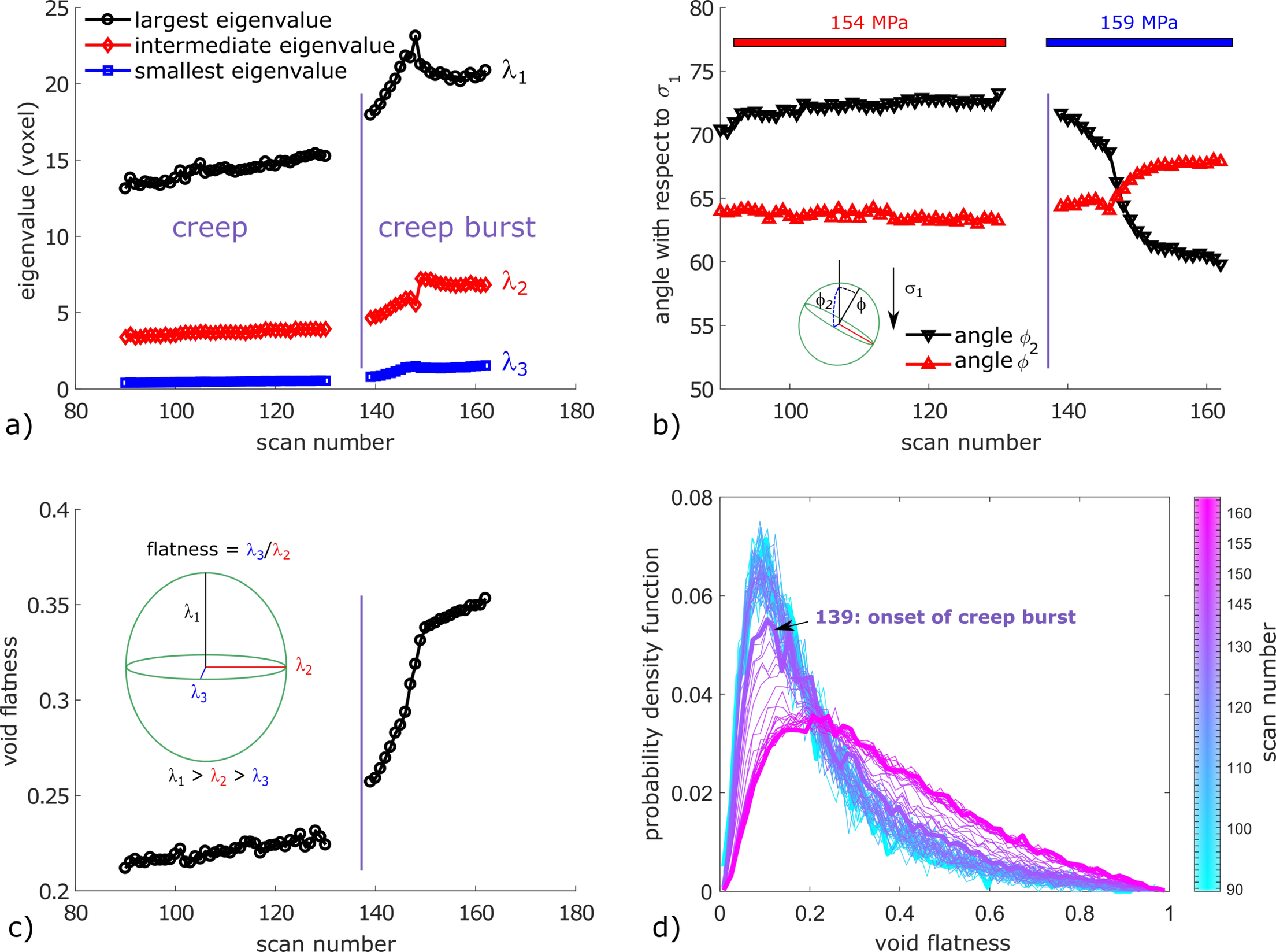
largest eigenvalue
intermediate eigenvalue
smallest eigenvalue
eigenvalue (voxel)
creep
creep burst
λ_1
λ_2
λ_3
scan number
a)
154 MPa
159 MPa
angle with respect to σ_1
ϕ_2
ϕ
σ_1
angle ϕ_2
angle ϕ
b)
flatness = λ_3/λ_2
$\lambda_1 > \lambda_2 > \lambda_3$
void flatness
c)
probability density function
139: onset of creep burst
void flatness
scan number
d)

Figure 10.

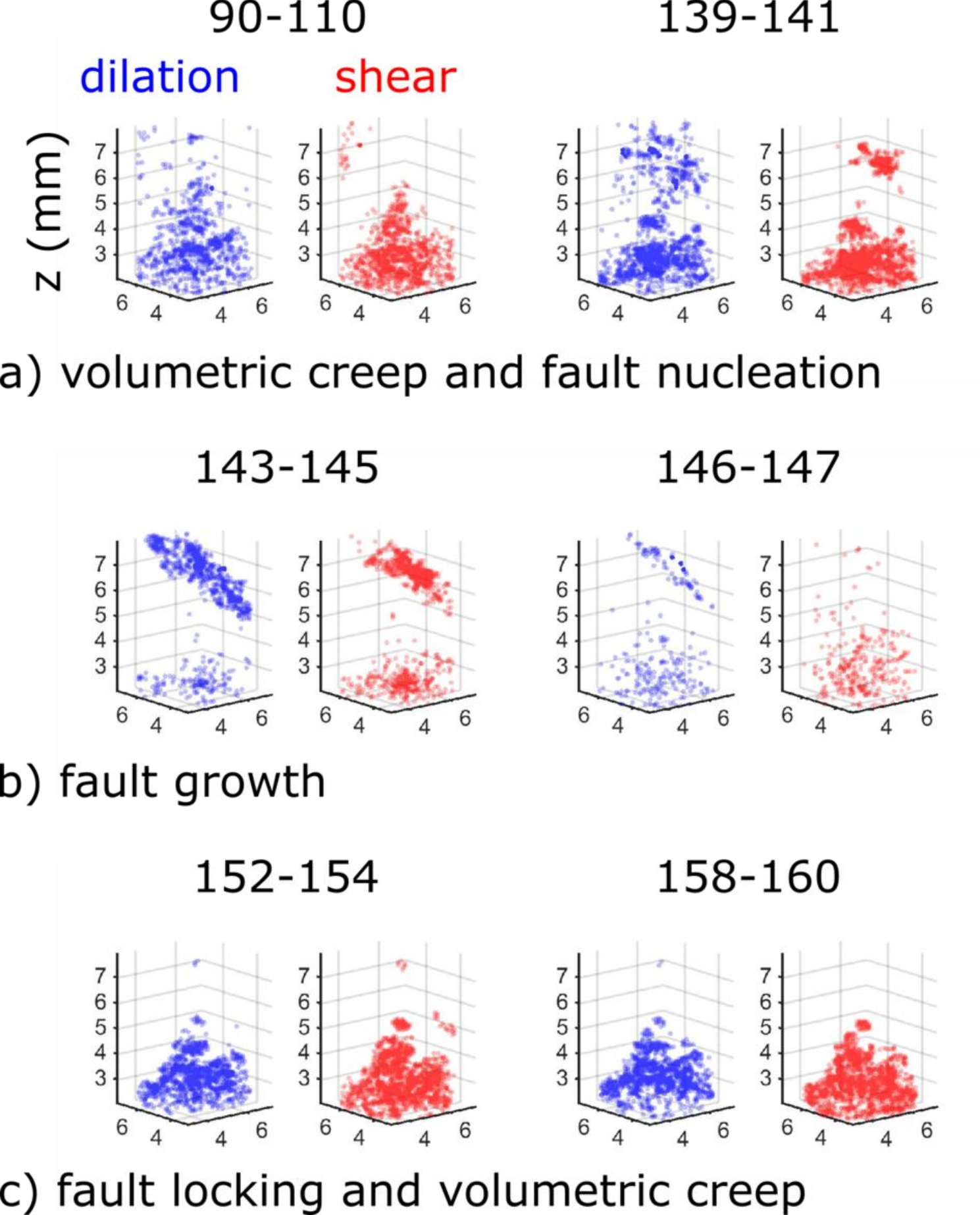
90-110
139-141
dilation
shear
z (mm)
a) volumetric creep and fault nucleation
143-145
146-147
b) fault growth
152-154
158-160
c) fault locking and volumetric creep

Figure 11.

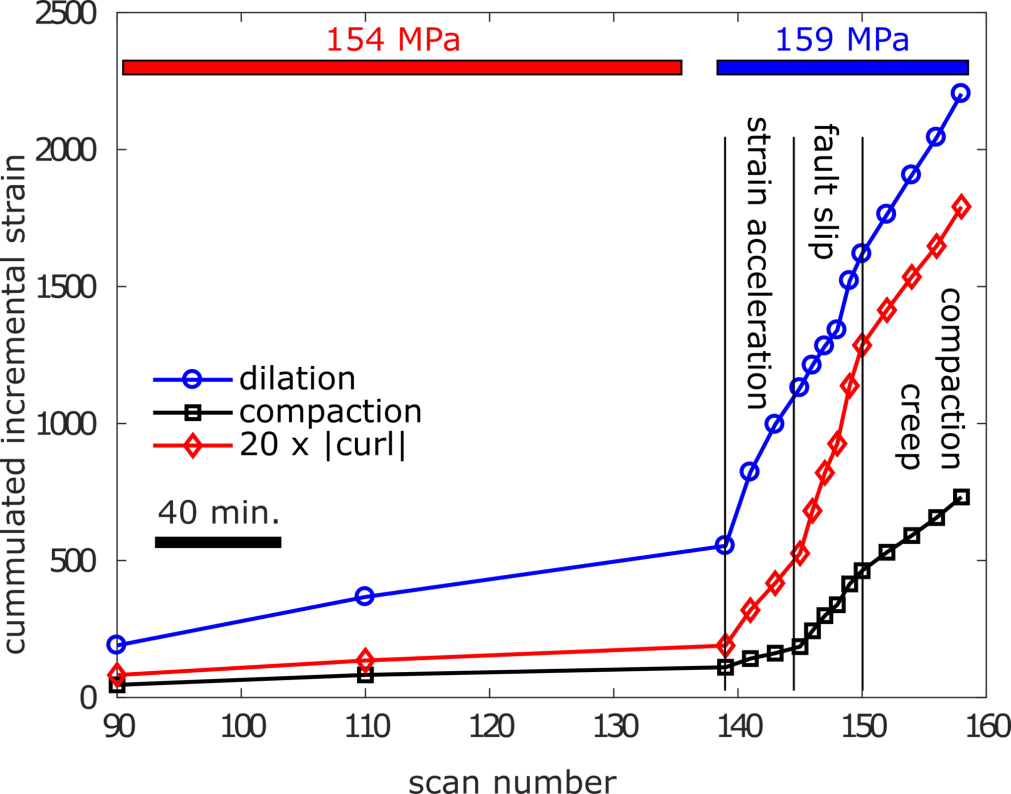
154 MPa
159 MPa
strain acceleration
fault slip
compaction creep
dilation
compaction
20 x |curl|
40 min.
cummulated incremental strain
scan number
0
500
1000
1500
2000
2500
90
100
110
120
130
140
150
160